

Magnetophonon Oscillations in Graphene with a Large Applied DC Bias Voltage



Joshua James Wengraf

**This dissertation is submitted for the degree of MSc by
Research**

September 2019

Declaration

This thesis has not been submitted in support of an application for another degree at this or any other university. It is the result of my own work and includes nothing that is the outcome of work done in collaboration except where specifically indicated. Many of the ideas in this thesis were the product of discussion with my supervisor Dr. Leonid Ponomarenko, Prof. Laurence Eaves, Dr. Mark Greenaway, Dr. Piranavan Kumaravadivel and Dr. Roshan Krishna Kumar. Theoretical support was provided by Dr. Mark Greenaway and Prof. Laurence Eaves.

Excerpts of this thesis have been published in the following academic publication:

Kumaravadivel P., Greenaway M. T., Perello D., Berdyugin A., Wengraf J., et al. Strong magnetophonon oscillations in extra large graphene (Supplementary Section 2). *Nature Communications*. 2019;10(1):3334.

Joshua Wengraf

Department of Physics,
Lancaster University, UK

Abstract

Magnetophonon resonance (MPR) oscillations are a valuable spectroscopic tool for studying electron interactions in solids. This type of spectroscopy is performed by applying a magnetic field to the solid, to quantise the energy of the charge carriers, and inter-Landau level scattering transitions are observed as oscillations in magnetoresistance. Since the transition energy is known, these oscillations can be used to identify phonons responsible for the inter-Landau level scattering. These oscillations, which arise due to scattering of Dirac fermions by transverse and longitudinal acoustic phonons, appear only in large graphene Hall bars with dimensions in excess of $10\ \mu\text{m}$ (greater than the phonon scattering mean free path). Here we apply large current-induced bias voltages (up to 1 mA) through a large graphene Hall bar and study the effect on the MPR oscillations. We observe a splitting of these oscillations due to a spatial tilting of the Landau levels induced by a strong Hall electric field. At sufficiently large Hall fields we also observe ‘phonon-less’ inter-Landau level scattering transitions which arise when the Landau level states become parallel in energy. Finally, we observe an additional scattering process when the drift velocity approaches the speed of the transverse acoustic phonon.

Acknowledgements

I would like to thank everyone for their help and advice over the past two years. We are shaped and moulded by our experiences and the people we meet, and I am grateful to the people in Manchester for helping me on my journey through the Centre for Doctoral Training (CDT). First and foremost, I would like to thank Irina for organising the course. This has been good to me. And I thank everyone within it who helped train me. Leonid Ponomarenko most of all. Leonid, your diligence and integrity is truly inspiring: I hope some of it has rubbed off on me. Roshan Krishna Kumar, thank you for setting me up in the group and for taking me through my first measurements with infectious enthusiasm. Mark Greenaway and Laurence Eaves, thank you for your continual support: you have been a constant source of inspiration. Piranavan Kumaravadivel, thank you for being my mentor and friend. Thank you to Mark and Dom for managing the cryostats with efficiency and flexibility. Qian (Qianny) Yang and Maddie Liberty Bella Howe, thank you for being a constant source of positive energy. You have helped me in more ways than you know. My thanks also to Prof. Sir. Andre Geim and Prof. Irina Grigorieva for settling me into the Manchester group and taking care of me thereafter. I would also like to thank Dr. Ivan Vera Merun, Mr. Alexey Berdyugin, Mr. Adam Draude, Dr. Artem Mishchenko, Dr. Stephen Church, Ms. Yulia Skliueva, Mr. Lucas Mogg, Ms. Livia Circa, Mr. Julien Barrier, Mr. Victor Hugo Guarochico Moreira, Dr. Minsoo Kim, Mr Rui Zhang, Mr. Wenjun Kuang, Mr. Michael Greaves, Mr. Tongcheng Yu, Miss Bonnie Tsim and Mr. Julien Barrier. Finally, I would like to thank Prof. Laurence Eaves, Dr. Leonid Ponomarenko, Mr. Julien Barrier, Miss Bonnie Tsim, and Mr. Peter Pihlmann Pederson for taking the time to proofread this thesis.

Contents

1	Introduction	1
1.1	Massless Dirac Fermions in Graphene	2
1.2	Electron Dynamics in a Magnetic Field	7
1.2.1	Magnetoresistance in Two Dimensions	7
1.2.2	Magnetic Focussing in Graphene	10
1.2.3	Landau Levels in Graphene	12
1.3	Phonons in Graphene	14
1.4	Magnetophonon Oscillations	16
1.4.1	Magnetophonon Oscillations in 2DEG's	16
1.4.2	Magnetophonon Oscillations in Graphene	20
2	Experimental Setup	27
2.1	Fabrication	27
2.2	Electrical Measurements	28
2.3	Sample Characterisation	30
3	Magnetic Focussing in Wide Graphene Hall Bars	35
4	Magnetophonon Oscillations in Graphene with a Large DC Bias	39
5	Conclusion and Outlook	48
	References	50

List of Figures

1.1	Crystal structure of graphene	4
1.2	Band structure of graphene	6
1.3	A schematic diagram of a Hall resistance measurement	8
1.4	A schematic diagram of a transverse magnetic focussing measurement	11
1.5	The quantum Hall effect in graphene	14
1.6	The phonon dispersion in graphene	15
1.7	Diagram of magnetophonon resonance in graphene	19
1.8	Hall-field induced resistance oscillations (HIRO) and magnetophonon oscillations in GaAs quantum wells	20
1.9	Diagram of magnetophonon resonance and Hall field-induced inter-Landau level tunnelling.	21
1.10	Magnetophonon oscillations in graphene	23
2.1	Picture of the cryostat and the electrical measurement equipment	29
2.2	Longitudinal resistance (R_{xx}) and differential resistance (dV/dI) measurement configurations	31
2.3	Longitudinal resistance and Hall resistance measurements over a range of gate voltages	33
2.4	Transverse magnetic focussing measurements	34
3.1	Magnetic focussing oscillations in the longitudinal resistance (R_{xx}) measurement configuration	37
4.1	Magnetophonon oscillations in Hall field-tilted Landau levels as a function of direct current at 40 K	41
4.2	Hall voltage as a function of direct current	43
4.3	Magnetophonon oscillations and Hall-field induced resistance oscillations (HIRO) as a function of direct current at 5 K	44
4.4	Hall field-induced resistance oscillations (HIRO) as a function of density with a direct current $I_{DC} = 250 \mu\text{A}$	46
4.5	Peak positions from Figure 4.4 plotted with the lines describing the positions of magnetophonon oscillations in Hall-tilted Landau levels and Hall field-induced resistance oscillations (HIRO).	47

List of Abbreviations and Acronyms

TMF: Transverse magnetic focussing

MPR: Magnetophonon resonance

SdH: Shubnikov de Haas

2DEG: Two-dimensional electron gas

PIRO: Phonon-induced resistance oscillations (also known as MPR oscillations)

HIRO: Hall-field induced resistance oscillations

MIRO: Microwave-induced resistance oscillations

Chapter 1

Introduction

This thesis reports my contribution to our recent discovery of magnetophonon oscillations in graphene. The unique band structure of graphene was first explored theoretically by Wallace in 1947 [1]. This led to the experimental discovery that charge carriers in graphene behave like relativistic Dirac fermions [2, 3], described by the Dirac equation rather than the Schrödinger equation, with the speed of light, c , replaced with the Fermi velocity, v_F [4]. Due to the atomic thickness of graphene the carrier density, n , can be tuned by a large extent ($n \sim 10^{12} - 10^{13} \text{ cm}^{-2}$) by the electric field effect [5]. Graphene has since been used to explore relativistic physics such as Klein tunnelling [6], and the success and versatility of graphene led to families of 2D Van der Waals crystals arranged in 2D heterostructures [7]. The electronic properties of these heterostructures were found to depend on both the stacking arrangement and the relative twist angle between different layers. In particular, in 2018, superconductivity was discovered in bilayer graphene with a specific twist angle of 1.1° between layers [8]. The precise mechanism for superconductivity in twisted bilayer graphene is not yet understood [9, 10].

Despite extensive studies of electronic transport in graphene over the past 15 years the magnetophonon effect, well known in other materials for over 50 years, has only recently been discovered [11]. Electron interactions with high energy phonons in graphene were only previously observed in Raman spectroscopy studies [12, 13]. This is because MPR is only observable in high quality graphene with spatial dimensions in excess of

10 μm [11]. MPR has been used to measure the low energy acoustic phonon dispersion in graphene. Although measurements of the full phonon dispersion curve have been made with inelastic X-ray scattering in graphite [14], MPR oscillations give a far more precise measurement of the low energy phonon dispersion [11]. In the experiment, we observed MPR arising from both transverse acoustic (TA) and longitudinal acoustic (LA) phonons. We also showed for the first time that Dirac fermions interact more strongly with the TA phonon than the LA phonon. Here we extend this work by studying MPR in graphene with large currents and thus large electric fields. We demonstrate that a strong Hall field tunes the energy of the MPR transitions, thereby allowing access to lower energy modes in the TA phonon dispersion. These low energy acoustic phonons might be relevant to the superconductivity mechanism in twisted bilayer graphene [9, 10]

This thesis is comprised of four chapters. Chapter 1 introduces the magnetophonon effect in graphene, building up from essential concepts of charge carrier and phonon transport. Chapter 2 reports our fabrication and electrical measurement methods; i.e., the alternating current (AC) and differential resistance measurements. Chapter 3 presents magnetoresistance measurements of magnetic focussing peaks in graphene, as discussed in our recent paper [11] (Supplementary Section 2)(see also a relevant theory paper by Greenaway et al. [15]). Finally, in Chapter 4, we present the new measurements of graphene MPR in large electric fields. We begin by discussing the known electronic properties of graphene.

1.1 Massless Dirac Fermions in Graphene

Graphene is a two-dimensional array of carbon atoms arranged in a hexagonal lattice. Each atom has six electrons, two of which form a $1s^2$ closed shell and the other four occupy hybridised $2s$, $2p_x$, $2p_y$ and $2p_z$ orbitals [16]. The four valence electrons form a

sp_2 hybridised state with three strong in-plane carbon bonds and one free out-of-plane p_z orbital. Only the out-of-plane p_z orbital contributes to electrical conduction in graphene.

Figure 1.1a shows the crystal structure of graphene. The unit cell consists of two atoms arranged in a parallelogram, spanned by lattice vectors, \vec{a}_1 and \vec{a}_2 , given by

$$\vec{a}_1 = a \left(\frac{1}{2}, \frac{\sqrt{3}}{2} \right) \quad \text{and} \quad \vec{a}_2 = a \left(\frac{1}{2}, -\frac{\sqrt{3}}{2} \right), \quad (1.1)$$

where the interatomic distance $a \approx 1.42 \text{ \AA}$ and the lattice period $|\vec{a}_1| = |\vec{a}_2| = \sqrt{3}a$ [4].

The corresponding reciprocal lattice vectors are given by

$$\vec{b}_1 = \frac{2\pi}{a} \left(\frac{1}{3}, \frac{\sqrt{3}}{3} \right) \quad \text{and} \quad \vec{b}_2 = \frac{2\pi}{a} \left(\frac{1}{3}, -\frac{\sqrt{3}}{3} \right). \quad (1.2)$$

These are shown in Figure 1.1b. Special high-symmetry points K, K', and M, lie at the edge of the Brillouin zone. These points are special because they describe standing waves with some special symmetry of the reciprocal lattice. Of particular interest are the K and K' points because they lie at the bottom of the K and K' valleys in the electronic dispersion.

Figure 1.2a shows the electronic dispersion of graphene calculated in the tight binding model [1]. The conduction and valence bands touch at the K and K' points, thus forming a gapless semiconductor. Near these points the electronic dispersion, $E(k)$, is linear; i.e.,

$$E \approx \pm v_F \hbar |k|, \quad (1.3)$$

where $v_F \approx 1 \times 10^6 \text{ ms}^{-1}$ is a constant known as the Fermi velocity [4], and k is the wavevector of the charge carrier. At low carrier densities ($n < 10^{10} \text{ cm}^{-2}$) v_F is renormalised to almost three times this value [17]. This energy spectrum is analagous to the photon dispersion, except with the speed of light, c , replaced with v_F , therefore low energy

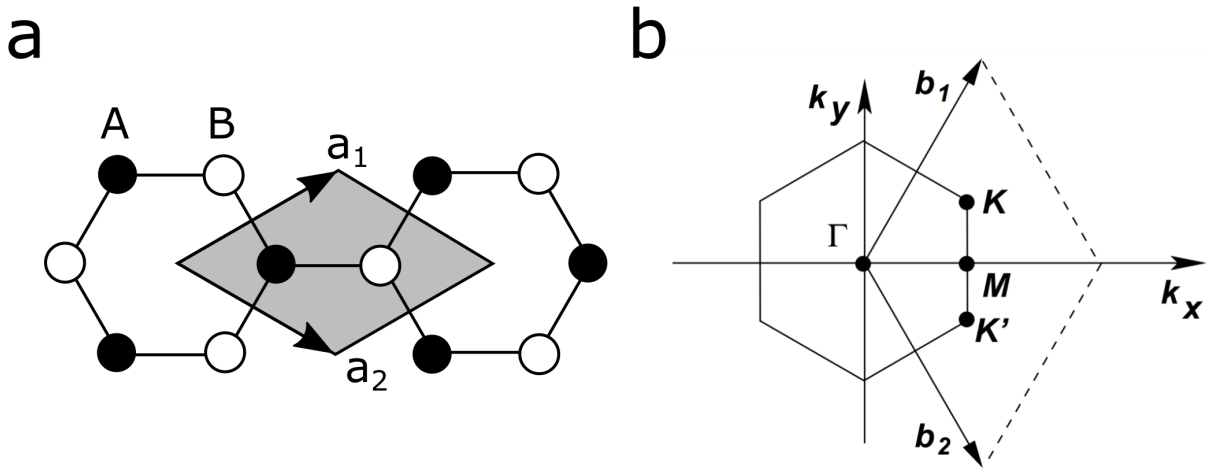


Figure 1.1: (a) Crystal structure of graphene formed of two intersecting triangular sublattices, A and B. Black coloured atoms represent the A sublattice and white coloured atoms represent the B sublattice. A shaded parallelogram depicts the conventional unit cell spanned by lattice vectors \vec{a}_1 and \vec{a}_2 . (b) The first Brillouin zone of graphene, obtained from [4]. Reciprocal lattice vectors \vec{b}_1 and \vec{b}_2 emanate from the Γ point at the centre of the Brillouin zone and special high symmetry points, K , K' and M , are shown at the edges.

electrons with wavevectors in the K and K' valleys behave as massless Dirac fermions [4].

As stated previously, each carbon atom donates one electron to the lattice and there are two atoms per unit cell. As a result there are two electrons per unit cell and so the Fermi level lies at the top of the valence band, at the K and K' points. This can be tuned by applying a gate voltage to either add or deplete electrons from the graphene. The K and K' valleys are also non-equivalent. As a result electrons have a degeneracy $g = g_s g_v = 4$, where $g_s = 2$ is the spin degeneracy and $g_v = 2$ is the valley degeneracy. This means up to 4 electrons can occupy each energy state in the electronic dispersion.

In equilibrium the carrier density, n , at energy E , is governed by the Fermi-Dirac distribution function, $f(E)$, given by

$$f(E) = \frac{1}{e^{(E-E_F)/k_B T} + 1}, \quad (1.4)$$

where E_F is the Fermi energy, k_B is the Boltzmann constant, and T is the temperature. This is plotted in Figure 1.2c. More specifically,

$$n = \int_{-\infty}^{E_F} N(E) f(E) dE, \quad (1.5)$$

where $N(E) \equiv dn/dE$ is the density of states. Electrons occupy energy states up to the Fermi level E_F . At finite temperature, electrons also occupy states of energies $\sim k_B T$ above E_F , and holes occupy states $\sim k_B T$ below E_F . Only electrons and holes with energies $\sim k_B T$ above or below E_F contribute to the electrical conductance in the graphene.

In graphene [16]

$$N(E) = g_s g_v \frac{E}{2\pi \hbar^2 v_F^2}, \quad (1.6)$$

since electrons occupy energy states $E = \hbar v_F k$ in a Fermi circle of radius k . In contrast to conventional 2D semiconductors, where $N(E)$ forms steps, the density of states in

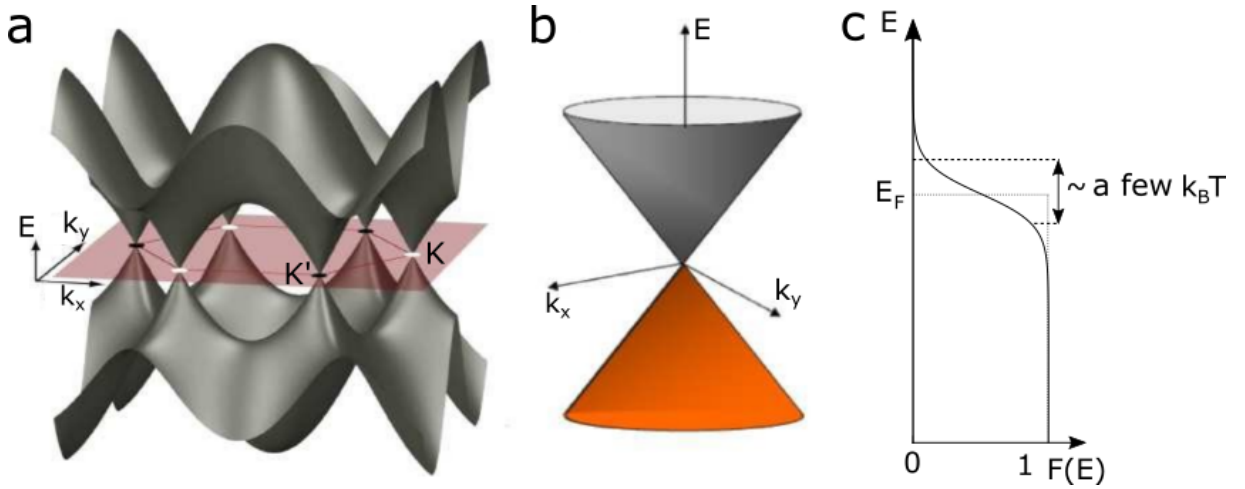


Figure 1.2: (a) The band structure of graphene, adapted from [19]. Two bands form valleys with a linear energy dispersion $E = \pm\hbar v_F |k|$ close to the K and K' points. (b) One of the low-energy valleys from (a). A black cone and an orange cone represent electron and hole states respectively. (c) The Fermi-Dirac distribution, $f(E)$, at finite temperature, T . The distribution $f(E)$ changes from $f(E) = 1$ (below E_F) to 0 (above E_F) across E_F in an energy range $\sim k_B T$.

graphene is linearly dependent on the energy.

In our recent publication [11] reporting MPR oscillations in graphene we measured at low currents ($\sim 1 \mu\text{A}$). Here we extend this work by applying large direct currents and thus large electric fields. The large electric field essentially injects ‘hot’ charge carriers with energies larger than the lattice temperature T ; i.e., larger than those predicted by the Fermi-Dirac distribution at this temperature. Charge carriers then relax towards the Fermi-Dirac distribution with a local temperature, $T = T(\vec{r})$, which depends on the position vector \vec{r} [18]. This idea is central to Chapter 4 of this thesis.

1.2 Electron Dynamics in a Magnetic Field

1.2.1 Magnetoresistance in Two Dimensions

In this thesis we measure electrical resistance in the Hall bar configuration. This configuration is depicted in figure 1.3. A current density, \vec{j}_x , is directed along the length of the Hall bar and a magnetic field, B , is applied perpendicularly. In general, the current, j_x , is given by a linear combination of the applied field, E_x , and the resultant Hall electric field, E_y :

$$j_x = \sigma_{xx}E_x + \sigma_{xy}E_y, \quad (1.7)$$

and

$$j_y = \sigma_{yx}E_x + \sigma_{yy}E_y = 0, \quad (1.8)$$

where σ_{xx} , σ_{xy} , σ_{yx} and σ_{yy} are components of the two dimensional conductivity tensor, $\boldsymbol{\sigma}$. In the Hall bar geometry current only flows in the x direction, thus $j_y = 0$. Assuming rotational symmetry, $\sigma_{xx} = \sigma_{yy}$ and $\sigma_{xy} = -\sigma_{yx}$ [20]; thus, equations (1.8) and (1.7) can be written as

$$\frac{E_y}{E_x} = \frac{\sigma_{xy}}{\sigma_{xx}} \quad (1.9)$$

and

$$j_x = \left(\sigma_{xx} + \frac{\sigma_{xy}^2}{\sigma_{xx}} \right) E_x, \quad (1.10)$$

respectively. In our experiment we apply current and measure electric field. We study the resistivity, $\boldsymbol{\rho}$, given by $\vec{E} \equiv \boldsymbol{\rho}\vec{j}$. Conductivity, given by $\vec{j} \equiv \boldsymbol{\sigma}\vec{E}$, is more useful when applying \vec{E} and measuring j_x . From equation (1.10), the resistivity $\rho_{xx} \equiv E_x/j_x$ can be

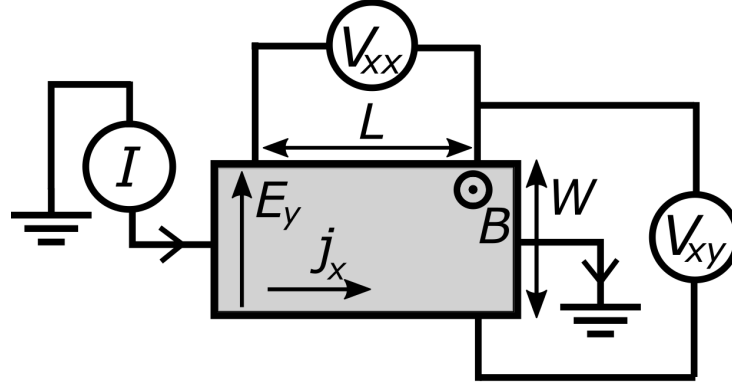


Figure 1.3: A schematic diagram of a longitudinal resistance (R_{xx}) and Hall resistance (R_{xy}) measurement of a Hall bar. A current density, j_x , is directed along the length of a Hall bar and a magnetic field is applied perpendicularly, producing a Hall electric field, E_y , directed across the width, W . Magnetoresistance, $R_{xx} \equiv V_{xx}/I$, where $I = j_x W$ is the current, is measured from a voltage, V_{xx} , across a length L .

rewritten as

$$\rho_{xx} = \frac{\sigma_{xx}}{\sigma_{xx}^2 + \sigma_{xy}^2}. \quad (1.11)$$

If $E_y \gg E_x$, as is the case for carriers with high mobility in a strong magnetic field, B , then, from equation (1.9), $\sigma_{xx} \ll \sigma_{xy}$. The resistivity can then be approximated as

$$\rho_{xx} \approx \frac{\sigma_{xx}}{\sigma_{xy}^2}. \quad (1.12)$$

Equation (1.12) is rather counter-intuitive. It states that the resistivity is proportional to the conductivity. This apparent paradox is resolved by recognising that ρ_{xx} is typically introduced with finite j_y and zero Hall field ($E_y = 0$).

In the Drude model the force on a carrier is given by the Lorentz force minus a momentum relaxation term:

$$\frac{d(m\vec{v})}{dt} = q(\vec{E} + \vec{v} \times \vec{B}) - \frac{m^*\vec{v}}{\tau}, \quad (1.13)$$

where \vec{v} is the carrier velocity, m^* is the effective mass, and τ is the relaxation time [21]. The relaxation time is a phenomenological parameter taken from experiment. In steady state the left hand side of equation (1.13) is zero; thus

$$\begin{pmatrix} E_x \\ E_y \end{pmatrix} = \begin{pmatrix} \rho_0 & B/ne \\ -B/ne & \rho_0 \end{pmatrix} \begin{pmatrix} j_x \\ j_y \end{pmatrix}, \quad (1.14)$$

where $\rho_0 = \sigma_0^{-1} = m^*/ne^2\tau$ and $(j_x, j_y) = -nev_d$, with a drift velocity \vec{v}_d . The mobility $\mu \equiv |\vec{v}_d|/|\vec{E}| = e\tau/m^*$ [21]. From equation (1.14), $\rho_{xx} \equiv E_x/j_x$ and

$$\rho_{xy} \equiv \frac{E_y}{j_x} = \frac{B}{ne}. \quad (1.15)$$

This is known as the Hall resistivity. Equation (1.15) is commonly used to calculate the carrier density n . Equation (1.14) can be written as

$$\begin{pmatrix} E_x \\ E_y \end{pmatrix} = \rho_0 \begin{pmatrix} 1 & \omega_c\tau \\ -\omega_c\tau & 1 \end{pmatrix} \begin{pmatrix} j_x \\ j_y \end{pmatrix}, \quad (1.16)$$

where $\omega_c \equiv eB/m^*$ is the cyclotron frequency. Comparing this with equation (1.9) gives $E_y/E_x = \sigma_{xy}/\sigma_{xx} = \omega_c\tau = \mu B$. This is equal to the number of cyclotron orbits completed before a scattering event. The condition $\sigma_{xy}/\sigma_{xx} = \omega_c\tau = \mu B \gg 1$ can therefore be interpreted as saying charge carriers complete multiple cyclotron orbits before scattering. This requires a high mobility and high magnetic field.

The longitudinal resistivity, ρ_{xx} , and Hall resistivity, ρ_{xy} , are calculated from the measured longitudinal resistance, R_{xx} , and Hall resistance, R_{xy} , as

$$R_{xx} \equiv \frac{\rho_{xx}W}{L}, \quad (1.17)$$

and

$$R_{xy} \equiv \rho_{xy}, \quad (1.18)$$

where W is the width of the Hall bar and L is the distance between voltage probes. These dimensions are shown in Figure 1.3.

1.2.2 Magnetic Focussing in Graphene

Transverse magnetic focussing (TMF) is the focussing of ballistic charge carriers onto voltage probes in the TMF configuration, as shown in Figure 1.4 [22]. In this configuration the current contact is perpendicular to the Hall bar and a positive voltage terminal is placed at distance, L , from the injector, with the other voltage terminal much further away. This is done so that it does not interfere with the voltage produced from TMF. If charge transport is ballistic; i.e., if charge carriers do not scatter along their trajectory, then they can be directed onto the voltage probe. This increases the carrier density in the vicinity of the voltage probe, thereby generating a potential difference. If charge transport is diffusive however; i.e., if charge carriers undergo diffusive motion, then their momentum will be randomised as they travel, and they will not reach the voltage terminal; they instead move down the applied potential gradient. A TMF voltage signal therefore indicates ballistic charge carriers have travelled through a region relatively free from defect scattering. At $B = 0$ T this information can be obtained in another configuration called the bend geometry [23].

In the semiclassical approximation, the force on a charge carrier, in a magnetic field \vec{B} , is given by

$$\hbar \dot{\vec{k}} = -e(\vec{v} \times \vec{B}), \quad (1.19)$$

where \vec{v} is the carrier velocity. When integrated with respect to time, at $E_F = \hbar v_F k_F$,

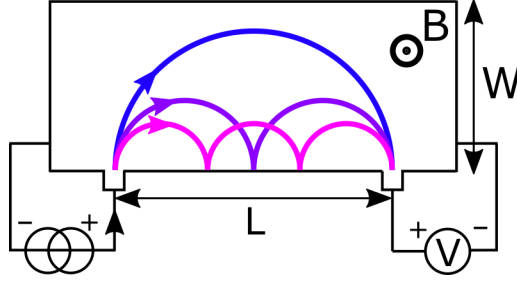


Figure 1.4: A transverse magnetic focussing measurement configuration. A current contact is perpendicular to the channel and a positive voltage contact is at a distance L from the injector. A perpendicular magnetic field B is applied. Three different magnetic focussing trajectories are shown, with $L = 2pR_c$ in blue, purple, and pink, for $p = 1, 2$ and 3 respectively.

this gives an equation of motion that describes cyclotron orbits with a radius, R_c , given by

$$R_c = k_F l_B^2, \quad (1.20)$$

where k_F is the Fermi wavevector and $l_B \equiv \sqrt{\hbar/eB}$ is the magnetic length. The cyclotron radius in real-space, R_c , is therefore equivalent to the cyclotron radius in k-space rescaled by l_B^2 . The Fermi wavevector $k_F = \sqrt{4\pi n/g_s g_v} = \sqrt{\pi n}$ can be increased by applying gate voltage to increase R_c . This has important consequences for MPR (and magnetic focussing) in graphene since R_c must be less than the lateral dimensions L and W to observe these oscillations [11].

If electrons are incident on the walls of the channel then they are specularly reflected. This results in skipping orbits along the boundary, as depicted in Figure 1.4. Ballistic charge carriers are focussed onto the voltage contact provided the distance between current and voltage probes $L = 2pR_c$, where p is an integer. This occurs at a

magnetic field, B_p , given by [24]

$$B_p = \frac{2\hbar\sqrt{\pi n}}{eL}p. \quad (1.21)$$

By varying n and B we can therefore measure B_p to find L . This can be compared with the distance measured with optical microscopy and as such can be used to prove charge carriers undergo ballistic motion.

1.2.3 Landau Levels in Graphene

At higher magnetic fields, when the cyclotron trajectories are closed ($\omega_c\tau \gtrsim 1$), the carrier wavefunction is confined; thus, energy is separated into discrete energy levels, known as Landau levels. The associated wavefunctions are solutions to the 1D harmonic oscillator [4]. In conventional semiconductors, the Landau levels are equidistant; i.e., $\Delta E_N = \hbar\omega_c$, where $\omega_c \equiv eB/m^*$, and m^* is constant around the bottom of parabolic conduction bands. In graphene however m^* is not a constant, but increases with energy according to $m^*v_F = \hbar k_F$, since the momentum $\hbar k_F = m^*v_g$ and $v_g = v_F$, where v_g is the group velocity in the graphene [25]. As a result, the inter-Landau level separation decreases with energy in graphene. More specifically, the Landau level energies are given by

$$E_N = \hbar\omega_c\sqrt{N}, \quad (1.22)$$

where $\hbar\omega_c = \sqrt{2\hbar v_F^2 eB}$. The Landau level energy separation, ΔE_N , decreases with N . As a consequence, the energy of inter-Landau level transitions in graphene can be tuned by both E_F and B .

In large enough B , when the energy spectrum separates into Landau levels, the density of states in equation (1.6) splits into a series of delta functions (broadened by scattering). As a result, the Landau levels are highly degenerate. The Landau level

degeneracy, g , is given by $g = g_s g_v / (2\pi l_B^2) = 4 / (2\pi l_B^2) = 4eB/h$; or equivalently, there are four electrons occupying any circle of radius l_B .

As energy is separated into Landau levels, the density of states forms peaks; these peak positions oscillate as a function of B . And, as the conductivity depends on the density of states at the Fermi level, this also oscillates as a function of B . These conductivity oscillations are known as Shubnikov-de Haas (SdH) oscillations. SdH oscillation maxima arise when the highest Landau level is completely filled; i.e., when $E_F = E_N$, or equivalently, when $n = in_s$, where i is an integer and $n_s = 4eB/h$ is the number of electrons per Landau level. SdH oscillation maxima therefore arise at magnetic fields, B_i , given by

$$B_i = \frac{nh}{4e} \frac{1}{i}. \quad (1.23)$$

As a result, the SdH oscillations are periodic as a function of $1/B$, with a periodicity given by $\Delta(1/B_i) = 4e/nh$. These oscillations can therefore be used to measure the carrier density, n . In reality the Landau levels are broadened by scattering, so the SdH oscillations are only observed when the energy broadening from the uncertainty principle, $\delta E = \hbar/\tau$, is much less than the Landau level energy separation, $\Delta E_N = \hbar\omega_c$; i.e., when $\omega_c\tau \gtrsim 1$.

At higher B , when the Fermi level is between largely separated Landau levels, ρ_{xx} vanishes and σ_{xy} forms plateaus at

$$\sigma_{xy} = \nu \frac{e^2}{h}, \quad (1.24)$$

where ν is the Landau level filling factor [3, 5]. In the usual quantum Hall effect, ν is equally spaced; however, in graphene, $\nu = 2, 6, 10, 14, \dots$. As a result the quantum Hall effect experimentally distinguishes graphene from other 2DEG's such as bilayer graphene [2, 3].

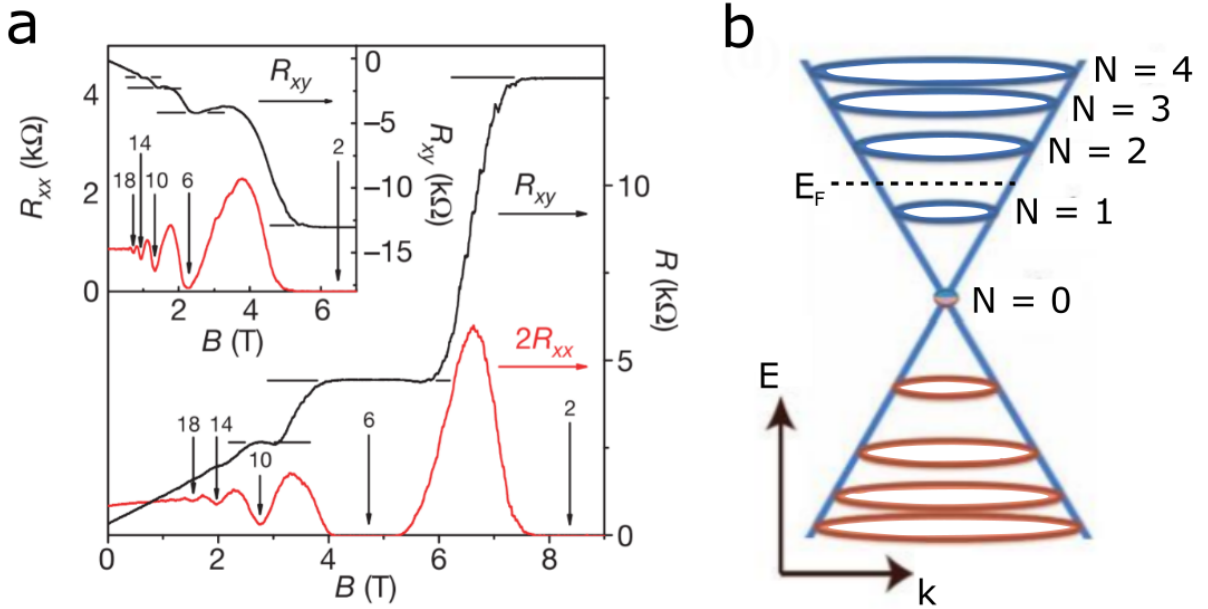


Figure 1.5: (a) $R_{xy} = R_{xy}(B)$ (black) and $R_{xx} = R_{xx}(B)$ (red) of graphene measured with $V_G = 15$ V and $V_G = -4$ V (inset) at 30 mK, obtained from [3]. Horizontal lines mark the quantum Hall plateaus and vertical arrows, labelled with $\nu = 2, 6$ and 10 respectively, mark the corresponding minima in R_{xx} . (b) Landau levels in graphene. Blue circles represent electron states and red circles represent hole states in the linear electronic dispersion. A Fermi level, E_F , is also shown.

Figure 1.5a shows the magnetoresistance of graphene measured by Zhang et al in 2005 [3]. In low B , $R_{xy} \propto B$ and $R_{xx} \approx \text{const}$. This is the classical Hall effect, as described in Section 1.2.1. At higher B ρ_{xx} develops into SdH oscillations, as discussed in this section. At higher $B \approx 3$ T these oscillations develop into a vanishing ρ_{xx} and three quantum Hall plateaus. This is the quantum Hall effect, as described by equation (1.24).

1.3 Phonons in Graphene

Figure 1.6 shows the phonon dispersion of graphene, calculated using atomic simulations [26]. Only the low momenta parts of the curves (near the Γ point) are relevant

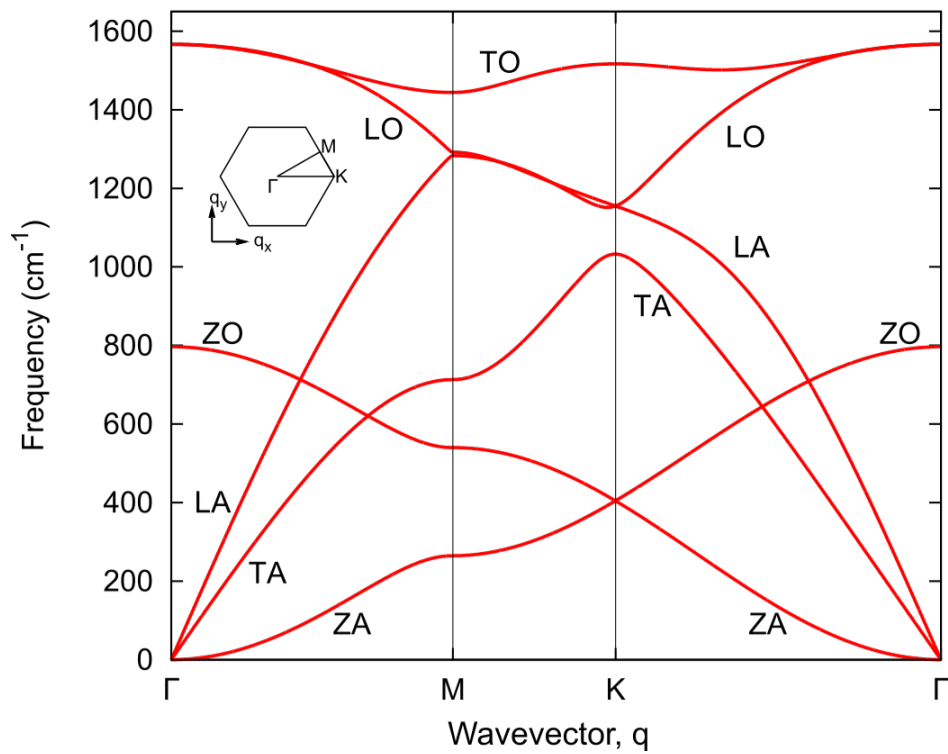


Figure 1.6: Phonon dispersion of graphene in units of cm^{-1} ($1 \text{ cm}^{-1} \equiv 0.124 \text{ meV}$), obtained from [26]. The inset shows the high symmetry points Γ , K and M in the first Brillouin zone.

for electron scattering processes contained within a valley. At such low momenta, optical phonons are essentially non-dispersed and acoustic phonons have a linear dispersion,

$$E \approx \hbar v_s k, \quad (1.25)$$

with a constant phonon velocity, v_s . Flatter sections of the dispersion curve have a higher density of states since $N(E) = N(k)dk/dE$. It is the transverse acoustic (TA) and longitudinal acoustic (LA) phonons which cause the MPR oscillations in graphene [11].

Phonons are bosons, so they are distributed according to the Bose-Einstein distribution function

$$f(E) = \frac{1}{e^{E/k_B T} - 1}. \quad (1.26)$$

In contrast to fermions, which may only occupy one energy state at a time, many phonons can occupy each energy state in the phonon dispersion. The total number of phonons present depends on the temperature, T . At low T the higher energy modes ‘freeze out’, since the majority of phonons occupy states of energy $E \lesssim k_B T$.

1.4 Magnetophonon Oscillations

1.4.1 Magnetophonon Oscillations in 2DEG’s

Magnetophonon oscillations, also known as phonon-induced resistance oscillations (PIRO), are oscillations in magnetoresistance due to phonon-induced inter-Landau level scattering. Magnetoresistance oscillations arise due to increased electron-phonon scattering when the phonon energy, E_p , matches the inter-Landau level energy separation, ΔE_N . These oscillations have been used extensively for studying the electron-phonon interaction in semiconductors: see Nicholas et al [27] (1985) and Dimitreiv et al. [28] (2012) for a

review.

Nicholas et al. [27] assumed MPR was induced only by optical phonons, at relatively high $T \sim 100$ K and high $B \sim 10$ T. Optical phonons have an approximately flat dispersion at low momenta (near the Γ point). This results in a fixed resonance condition at a fixed phonon energy, E_p , given by

$$E_p = p\hbar\omega_c, \quad (1.27)$$

where p is an integer. MPR was also observed at lower temperatures ($T < 5K$) in large electric fields. As discussed previously, large electric fields inject ‘hot’ carriers with energies greater than the lattice temperature. These carriers predominantly relax, thereby enhancing the MPR oscillations. It is worth noting that this enhancement can also be attributed to Joule heating. In addition, at such large electric fields, new scattering processes were observed as a shift in the MPR peak positions, due to a shift in the MPR condition.

The review by Dimitreiv et al. [28] in 2012 focussed on acoustic phonon-induced MPR oscillations with a fixed momentum transfer $q \approx 2\hbar k_F$. This type of oscillation is only observed in materials with a high carrier mobility μ . Acoustic MPR arise at lower T ($T \sim 10$ K) and lower B ($B \sim 1$ T) than optical phonon-induced MPR [29]. Since acoustic phonon energy $E_p = qv_s = p\hbar\omega_c$ and $q \approx 2\hbar k_F$, acoustic MPR oscillations can be used to measure the phonon speed, v_s . Figure 1.7 depicts the MPR condition in graphene. Acoustic phonons of energy $E = qv_s = 2\hbar k_F v_s$ backscatter the charge carriers, which results in a momentum shift $q \approx 2\hbar k_F$ and thus a shift of the orbital guiding centre by a distance $\Delta y \approx 2R_c \equiv 2k_F l_B^2$, from equation (1.20). This is the most likely transition, because, at this distance, the initial and final harmonic oscillator wavefunctions have maximal overlap [30]. A $2\hbar k_F$ momentum transfer is also argued as the transition with the most available phase space. In graphene however, this leads to $q \approx \hbar k_F$ rather than $q \approx 2\hbar k_F$ [31]. As discussed by Dimitreiv et al [28], three types of magnetoresistance oscillations have been

observed with a momentum shift $q \approx 2\hbar k_F$, namely the phonon-induced resistance oscillations (PIRO)(also known as MPR oscillations), Hall field-induced resistance oscillations (HIRO), and microwave-induced resistance oscillations (MIRO). PIRO and HIRO are the subject of this thesis.

Acoustic MPR oscillations were first observed by Zudov et al. in 2001 [30, 32]. These oscillations have been discovered in bulk Ga and Si [33] and 2DEG's [34]. They have previously been used to measure phonon velocities in these materials, however the interacting phonon modes are not well established [35, 29]. A defining feature of MPR oscillations is their amplitude as a function of temperature: the amplitude increases up to a certain critical temperature (at around 90 K), and then decreases at higher temperatures. This critical temperature increases with B [36]. At lower temperatures, the amplitude is smaller due to a lack of available phonons and empty states to scatter into. At higher temperatures, the amplitude decreases when the Landau level energy broadening, $\delta E = \hbar/\tau$, becomes similar to the Landau level separation, $\Delta E_N = \hbar\omega_c$; or equivalently, when $\omega_c\tau \lesssim 1$.

HIRO are essentially a phonon-less analogue of PIRO. These oscillations arise when Landau level energy states, tilted by the Hall field, become parallel in energy at $q \approx 2\hbar k_F$. The momentum transfer $q \approx 2\hbar k_F$ is provided by impurities in the lattice [28]. HIRO have been used to measure both the quantum lifetime and backscattering rate in 2DEG's [37]. Surprisingly, the amplitude of HIRO have been shown to increase with density when a new sub-band becomes populated. This is thought to be attributed to an enhancement of the quantum lifetime due to impurity screening [38]. HIRO have been discovered in many other 2DEG's such as Si/GeSi [39] and MgZnO heterostructures [40], with a wide range of carrier densities and mobilities.

In 2008, Zhang et al. [29] studied MPR with a large direct current passing through a wide 2DEG Hall bar. They discovered that the resultant Hall electric field splits the MPR

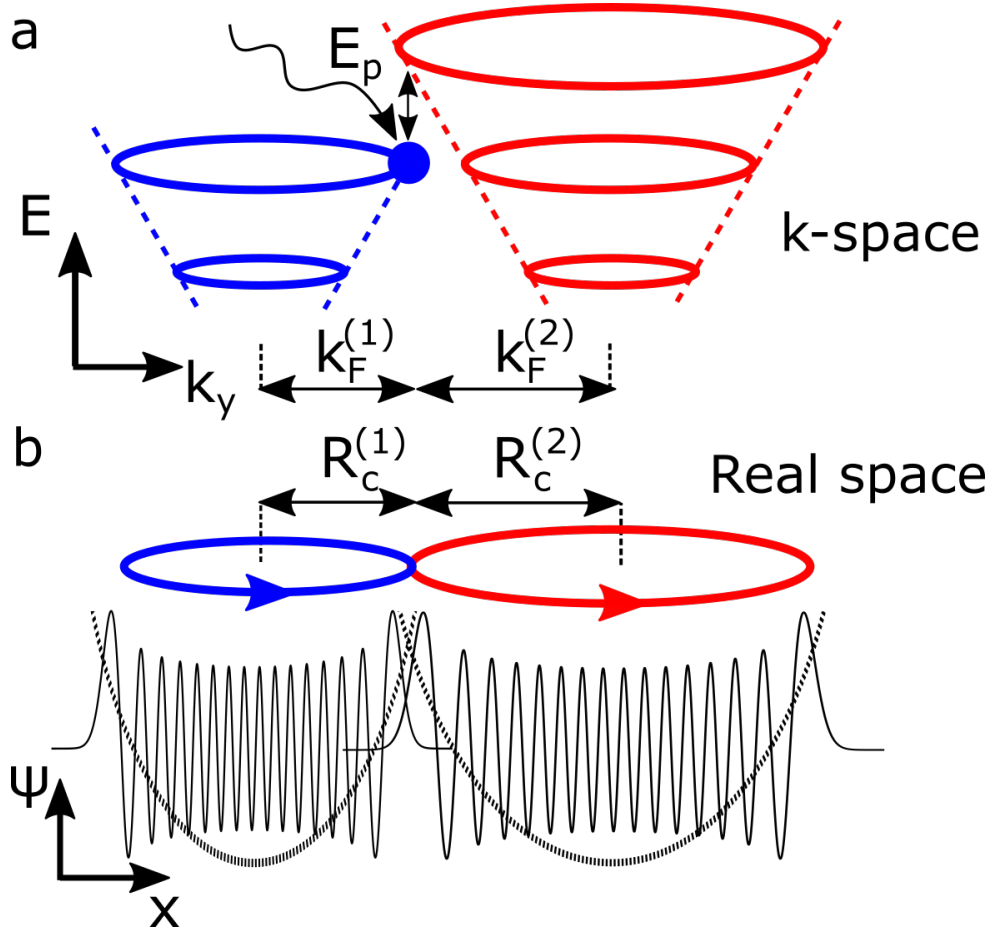


Figure 1.7: Diagram of the MPR condition in graphene. (a) A phonon of energy E_p incident on a charge carrier induces a transition from an occupied Landau level (blue) with momentum $\hbar k_F^{(1)}$ to an unoccupied Landau level (red) with momentum $\hbar k_F^{(2)}$. (b) Semiclassical diagram of the MPR condition in real space. The MPR transition induces a shift from a cyclotron orbit of radius $R_c^{(1)}$ (blue) to a cyclotron orbit of radius $R_c^{(2)}$ (red). Solid black lines depict the associated harmonic oscillator wavefunctions and dotted black lines depict the corresponding harmonic oscillator potential. Tails of the two harmonic oscillator wavefunctions overlap when the cyclotron orbits touch in real-space.

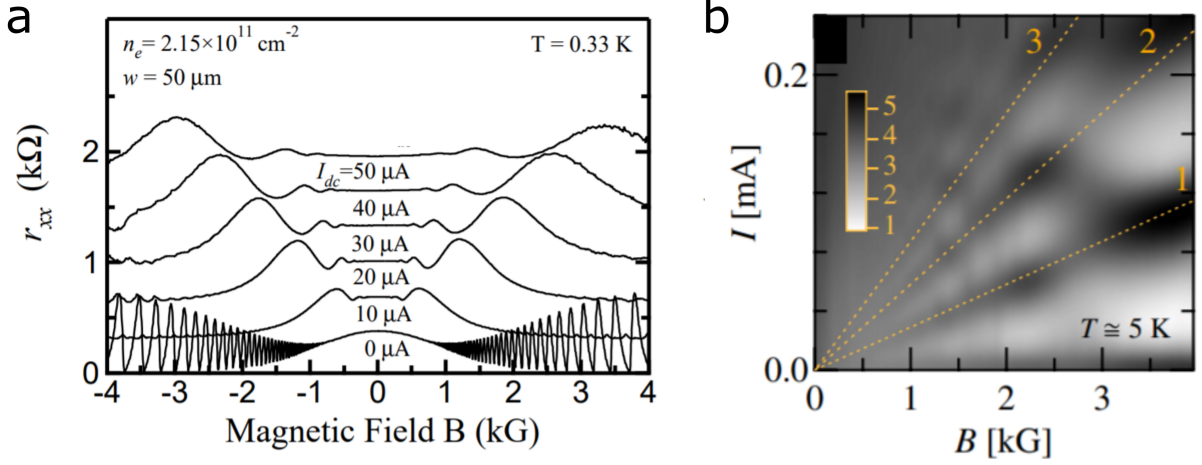


Figure 1.8: (a) HIRO in a GaAs quantum well from $I_{DC} = 0 \mu\text{A}$ to $I_{DC} = 50 \mu\text{A}$ at intervals $\Delta I_{DC} = 10 \mu\text{A}$ at 0.3K; adapted from [41]. (b) A grayscale plot of $dV/dI \equiv r_{xx} = r_{xx}(B, I_{DC})$ of HIRO and PIRO in a GaAs quantum well, at 5K; obtained from [29]. Yellow dotted lines mark HIRO with integers $q = 1, 2$ and 3 , where q is the change in Landau level index. [Note $1\text{kG} = 0.1\text{T}$].

peaks, and also induces a zero resistance state. This MPR peak splitting is attributed to a spatial tilting of the Landau levels in a strong Hall field E_y , which shifts the MPR condition by energies $\Delta E = \pm 2eR_c E_y$. This Landau level tilting is depicted in Figure 1.9. Zhang et al. also observed HIRO embedded in the split MPR oscillations. Furthermore, at higher current, they observe a new resistance peak arising when the drift velocity approaches the speed of a phonon; i.e., when Landau levels become parallel to the phonon dispersion. This opens up a new scattering channel as many phonons satisfying energy-momentum conservation become available. These features are discussed in Section 4 of this thesis.

1.4.2 Magnetophonon Oscillations in Graphene

Acoustic MPR oscillations have only recently been discovered in graphene, despite exceptionally high carrier mobilities. This is because, as we have shown in [11], they require large Hall bars with dimensions greater than the phonon scattering mean free

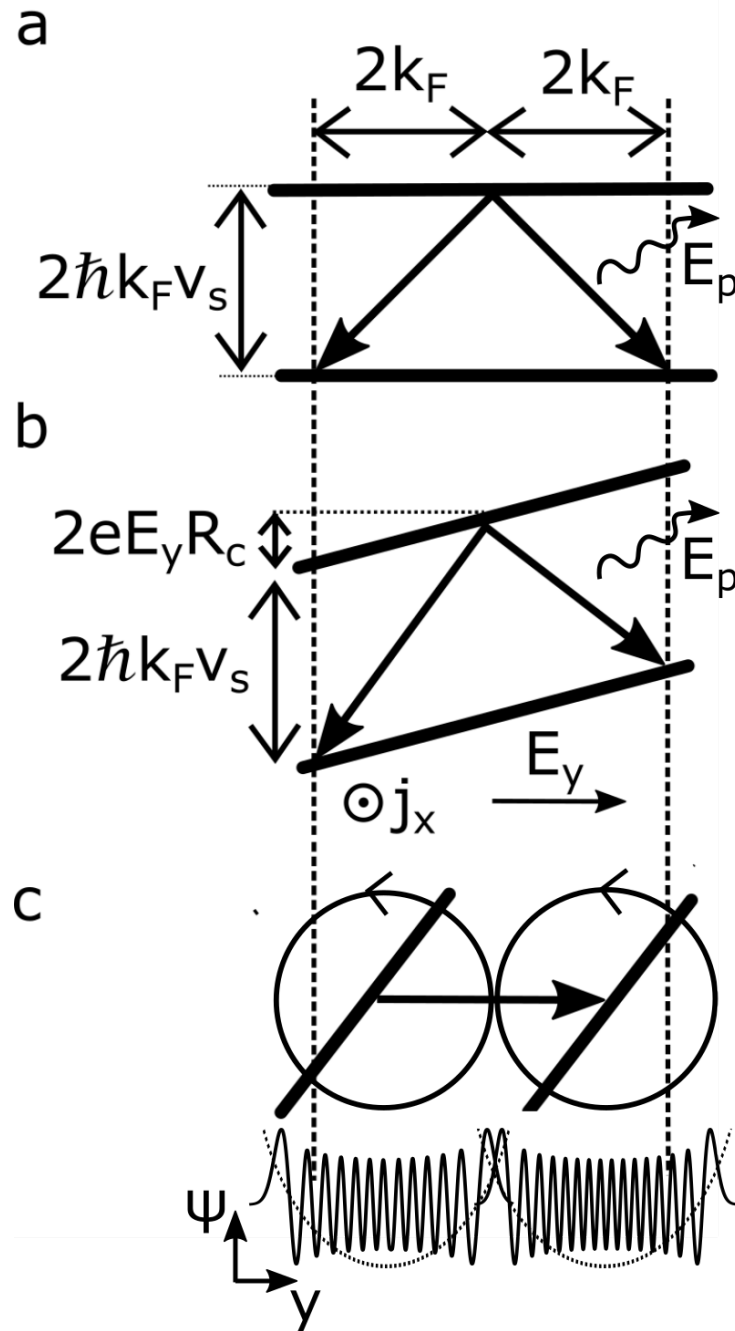


Figure 1.9: (a) Diagram of MPR transitions in real space, from a higher Landau level to a lower one, with a momentum transfer $\vec{q} = \pm 2\hbar\vec{k}_F$ and energy $E = v_s|q|$. (b) Diagram of MPR transitions between Landau levels tilted by a Hall electric field, E_y , induced by a current density, j_x , directed into the page. The two transitions are shifted in energy by $\pm 2eE_y R_c$. (c) A transition between Hall-field tilted Landau level states which are aligned in energy at $q = 2\hbar k_F$. Black circles represent cyclotron orbits which touch in real space. The associated harmonic oscillator wavefunction and harmonic oscillator potential are drawn in solid black and dotted black, respectively.

path. Previous to this discovery, Mori and Ando predicted optical phonon-induced MPR due to both inter-valley scattering, by low-momentum phonons close to the Γ point, and intra-valley scattering, by high-momentum phonons near the K point [42], however these are yet to be measured.

Figure 1.10 shows MPR oscillations in graphene as a function of temperature, as presented in our recent paper [11], at a fixed hole carrier density $n = 3.2 \times 10^{12} \text{ cm}^{-2}$. These oscillations are marked by $p = 1, 2, 3, 4$ and 5 respectively. There are also two other types of oscillation present with a distinctly smaller frequency. These are the SdH oscillations (at low $T \approx 5\text{K}$) and magnetic focussing oscillations (at low $B < 0.3\text{T}$). The SdH oscillations were confirmed by comparing n calculated from the SdH oscillation period (using equation (1.23)), to n calculated from the Hall voltage. The magnetic focussing oscillations are confirmed in Section 3 of this thesis. As the temperature is increased, both the SdH oscillations and magnetic focussing oscillations are suppressed and the MPR oscillations emerge, eventually fading again at $T \gtrsim 110\text{K}$, when $\omega_c\tau \lesssim 1$. The Fermi velocity, $v_F = (1.06 \pm 0.05) \times 10^6 \text{ ms}^{-1}$, was extracted from the amplitude of the SdH oscillations, as shown in [11], and the phonon speed $v_s = 13.6 \pm 0.7 \text{ kms}^{-1}$ was extracted by fitting the MPR oscillation peak positions to the MPR resonance condition (shown in equation (1.31)), using this value of v_F . This is consistent with the theoretically calculated TA phonon velocity $v_s \sim 13 \text{ kms}^{-1}$ [43, 44, 26]. The LA phonon was observed as a small shoulder peak. These observations prove that MPR is predominantly due to TA phonons. Greenaway et al. [15] produced a theoretical model to explain why Dirac fermions scatter with TA phonons rather than LA phonons in graphene. They discovered it is, in part, due to carrier screening of the deformation potential. We also studied MPR in graphene with different lateral sizes, and found MPR oscillations are only observed in graphene with lateral size $L \gtrsim 10 \text{ }\mu\text{m}$ (greater than the phonon limited mean free path).

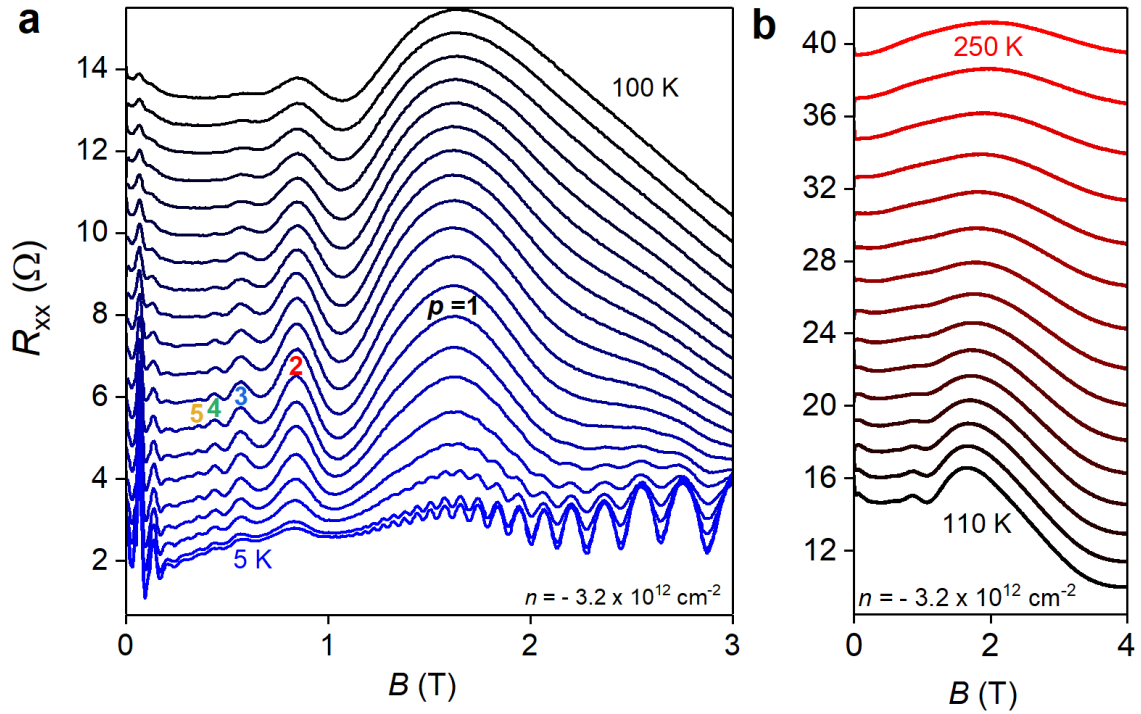


Figure 1.10: (a) MPR oscillations of the graphene studied in this thesis with a small AC excitation current $I_{AC} \sim 1 \mu\text{A}$ from 5 K to 100 K at intervals $\Delta T = 5$ K, at a hole carrier density $n = 3.2 \times 10^{12} \text{ cm}^{-2}$. MPR oscillation peak positions are marked by $p = 1, 2, 3, 4$ and 5 respectively. (b) Extended dataset of (a) from 110 K to 250 K with intervals $\Delta T = 10$ K.

1.4.2.1 MPR in Graphene

In the semiclassical approximation, the cyclotron radius, R_c , of a charge carrier in Landau-quantised graphene is given by [15]

$$R_c = l_B \sqrt{2N}. \quad (1.28)$$

As before, acoustic MPR transitions have a spatial displacement $\Delta Y = R_c^{(1)} + R_c^{(2)} \approx 2R_c$ and a momentum transfer $q = \hbar |\vec{k}_N^{(1)} - \vec{k}_N^{(2)}| \approx 2\hbar k_F$, where we have used equation (1.20) to convert between real and momentum space. Landau level transitions occur when the phonon energy, $E_p = v_s q$, matches Landau level separation, $E_p = \Delta E_N$; i.e. when

$$2\hbar v_s k_F = \pm v_F \sqrt{2\hbar e B_p} (\sqrt{N \pm p} - \sqrt{N}), \quad (1.29)$$

where p is the change in the Landau level index and B_p is the magnetic field at resonance. Since n gives momentum transfer $q = 2\hbar k_F = 2\hbar \sqrt{\pi n}$, and B gives ΔE_N , we can tune n and B to find B_p . MPR oscillations occur at a Landau level index, N_p , given by [11]

$$N_p = \frac{p v_s}{4 v_F} \left(\frac{v_F}{v_s} - 1 \right)^2 \approx \frac{p v_F}{4 v_s}. \quad (1.30)$$

This is calculated from equation (1.29) using the approximation $v_F \gg v_s$. Since ΔE_N decreases with N , N_p can be thought of as a critical Landau level index, below which MPR cannot occur. For the observed MPR in graphene, $N_p \sim 20$ for $p = 1$ [11]. Furthermore, since $E_F = E_N$, the N th Landau level is filled, so $n = 4NeB/h$. Equation (1.30) is therefore equivalent to

$$B_p = \frac{\hbar v_F}{e v_s} \left(\frac{v_F}{v_s} - 1 \right)^{-2} \frac{1}{p} \approx \frac{\hbar v_s}{e v_F} \frac{1}{p}. \quad (1.31)$$

Electron-phonon scattering is maximal when equation (1.31) is satisfied, thus the MPR oscillations are periodic as a function of $1/B$, with a periodicity given by $\Delta(1/B) = ev_F/n\hbar v_s$.

1.4.2.2 MPR With a Large Direct Current

When a large direct current, I_{DC} , flows through the graphene Hall bar, the Landau level energy states are spatially tilted by a strong Hall electric field, E_y . This is depicted in Figure 1.9b. The MPR energies are shifted as electrons travelling a distance $2R_c$ either gain or lose an energy $\Delta E = 2eE_yR_c$, by absorbing or emitting a photon from the Hall electric field. The MPR condition in equation (1.29) therefore becomes

$$2\hbar v_s k_F = \pm v_F \sqrt{2\hbar e B_p} (\sqrt{N \pm p} - \sqrt{N}) \pm 2eE_y R_c. \quad (1.32)$$

We write $E_y = \rho_{xy} j_x = [\nu(e^2/h)]^{-1} j_x$, where e^2/h is the conductance quantum and $\nu = g_s g_v N \approx 4N$ is the Landau level filling factor at large N . In the $v_F \gg v_s$ approximation, equation (1.32) becomes

$$B_p \approx \left(\frac{n\hbar v_s}{ev_f} \pm \frac{\hbar}{e^2} \frac{I_{DC}}{v_F W} \right) \frac{1}{p}, \quad (1.33)$$

where W is the width of the device. This splitting of the resonance condition is observed in Chapter 4.

At sufficiently large current, when Landau level states are aligned in energy at $q \approx 2\hbar k_F$, electrons make elastic inter-Landau level transitions using the Hall electric field only; i.e., without absorbing or emitting a phonon. This situation is depicted in Figure 1.9c. The idea was discussed theoretically by Eaves and Sheard in 1986 [45]. In this case

equation (1.32) becomes

$$2eE_y R_c = \pm v_F \sqrt{2\hbar e B_q} (\sqrt{N \pm q} - \sqrt{N}), \quad (1.34)$$

where B_q is the magnetic field at resonance, and q is the change in Landau level index. Following the same analysis as above, we have

$$B_q = \frac{h}{e^2} \frac{I_{DC}}{v_F W} \frac{1}{q}. \quad (1.35)$$

Inter-Landau level scattering arises when equation (1.35) is satisfied; thus, the resultant HIRO are periodic as a function of $1/B$, with a periodicity given by $\Delta(1/B) = e^2 v_F W / h I_{DC}$.

In the MPR condition, given by equation (1.31), B_p is proportional to n and independent of I_{DC} ; whereas in the HIRO condition, given by equation (1.35), B_q is proportional to I_{DC} and independent of n . As a result, we can distinguish these two types of oscillation by their dependence on n and I_{DC} .

Chapter 2

Experimental Setup

2.1 Fabrication

The graphene Hall bar under test was fabricated by Piranavan Kumaravadivel [11]. This Hall-bar is shown in Figure 2.1e. It consists of hexagonal Boron Nitride (hBN) encapsulated graphene and has one dimensional gold contacts, where only the edge of the graphene is in contact with the gold [46]. The bottom hBN layer serves as atomically flat substrate for the graphene to rest on and the top hBN layer protects the graphene from impurities and polymers used in fabrication. The fabrication process is described as follows. First, a SiO₂ substrate was cleaned by an O₂ and Ar plasma. Graphene and hBN were then mechanically exfoliated with low-tack sticky tape. The graphene and hBN (of thicknesses 25 nm to 100 nm) were then identified using an optical microscope with dark-field imaging. Next, polypropyl carbonate (PPC) was spin coated on a polydimethylsiloxane (PDMS) stamp. Using a xyz micromanipulator, the PDMS stamp was then used to pick up the hBN at a substrate temperature of 50°C. This was then used to pick up the graphene with a substrate temperature of 65°C. Finally, the hBN-graphene heterostructure was deposited on the bottom hBN layer at a substrate temperature 65°C.

Next, the heterostructure was shaped into a Hall Bar using electron beam lithography. A polymethyl methacrylate (PMMA) resist was patterned on the heterostructure and the Hall bar region was exposed to an electron beam. Reactive ions (CHF₃ + O₂)

were then used to etch regions outside the Hall bar region. Gold (Au) and copper (Cu) (in the ratio 70:5 by thickness) was then deposited using physical vapour deposition to create the contacts [46]. The rest of the Hall bar was then shaped using electron beam lithography with a PMMA mask and reactive ion etching, as before.

2.2 Electrical Measurements

All of the electrical measurements presented in this thesis were performed in a CH Series helium gas flow cryostat with a superconducting magnet capable of reaching fields of 15 T perpendicular to the graphene plane. First, the graphene Hall bar was placed on the top of a long insert. This insert is shown in Figure 2.1d. The insert was then capped with a metal cover, sealed with vacuum grease, and pumped to ultra high vacuum ($\sim 10^{-5}$ mbar) to protect the graphene from contaminants in the helium. The insert was then placed in the cryostat. Using a variable temperature insert (VTI) capable of operating in a temperature range between 2 K and 400 K, helium-4 (^4He) was pumped across the device from the outer chamber of the cryostat to cool the graphene. A Mercury-iTC temperature controller was then used to monitor and control the temperature of the ^4He gas. The helium flow rate was controlled with a needle valve and monitored with a vacuum gauge. The helium level was monitored by resistance measurements of a superconducting wire running down the length of the cryostat. A Mercury-IPS power supply was used to generate the magnetic fields in the superconducting magnet.

After the graphene was cooled by He gas flow for approximately 1 hour we began the electrical measurements. Voltage, V , was measured using a SR380 lock-in amplifier operating at a frequency $f \approx 30$ Hz, with a small AC excitation current $i \sim 1$ μA . This current was sourced by applying a voltage from the lock-in amplifier across a 1 M Ω resistor. This resistor ensures an approximately constant current amplitude for typical graphene

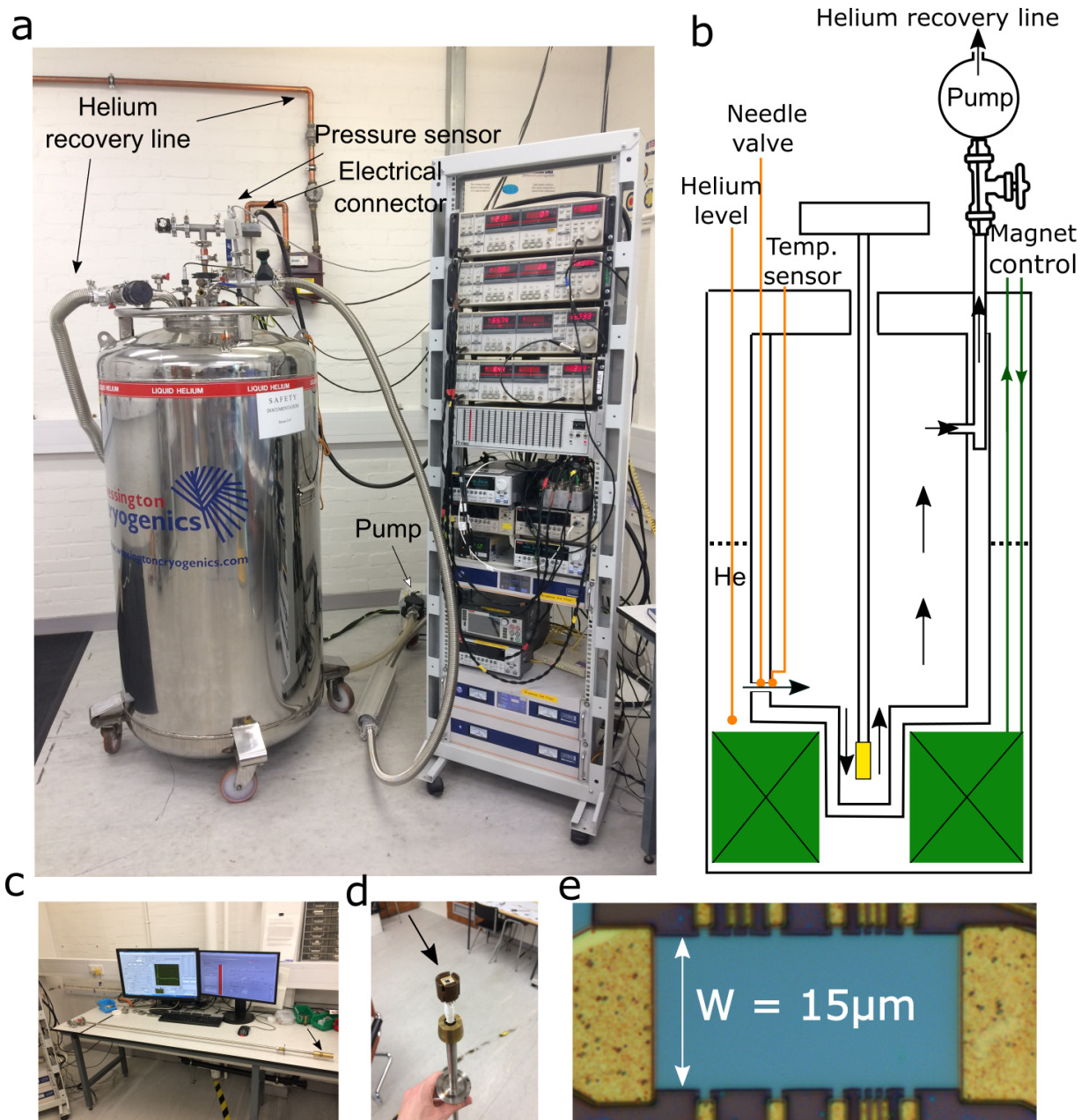


Figure 2.1: (a) A photograph of the cryostat and electrical equipment used to measure the device. Arrows mark the location of the pump, helium recovery line, pressure sensor, and electrical connection. (b) Schematic diagram of the flow cryostat in operation. Arrows show the direction of helium flow, across the device and then to the recovery line. Green boxes show the position of the superconducting magnet. (c) Photograph of the insert capped with a metal cover. (d) Photograph of the insert. (e) Photograph of the graphene Hall bar under test taken with an optical microscope.

resistances $R \lesssim 1 \text{ k}\Omega$. A gate voltage, V_G , was applied across the bottom Si/SiO₂/hBN substrate to add charge carriers to the graphene: a positive V_G was applied to add electrons and a negative V_G was applied to add holes. Figure 2.2a shows the configuration used to measure resistances presented in Chapter 3. Figure 2.2b shows the configuration used to measure differential resistances presented in Chapter 4. In this configuration a DC current, $I_{DC} \sim 100 \mu\text{A}$ was added to a small AC current $i = 2 \mu\text{A}$. DC current was sourced by applying a DC voltage from a Keithley 2400 sourcemeter across a $100 \text{ k}\Omega$ resistor. The AC voltage was measured with AC coupling to prevent large DC induced bias voltage from overloading the lock-in amplifier. With a small AC current $i \ll I$, where $I = I_{DC}$, the voltage is given by

$$V(I + i \sin \omega t) = V(I) + \frac{dV}{dI} i \sin \omega t + \dots; \quad (2.1)$$

i.e., a large DC voltage $V(I)$ plus a small AC voltage. The AC voltage amplitude, $i dV/dI$, is measured with the lock-in amplifier operating at the same frequency as the applied AC voltage. The differential resistance, dV/dI , is calculated from this by dividing by the current amplitude, i . This is equal to the derivative of $V(I)$. The AC voltage is induced to provide a baseline for the lock-in amplifier to measure the derivative of $V(I)$. The differential resistance measurement is far more sensitive to small changes in resistance, furthermore it is better to measure the slope of $V(I)$ directly than to calculate the derivative, since taking the derivative of any measured data will amplify the noise and thus hide the signal of interest. DC resistance can be calculated from any measured dV/dI by integrating with respect to $I = I_{DC}$.

2.3 Sample Characterisation

First we measured the resistance of the graphene at low current bias to check its electronic quality. We calculated the carrier density n from the Hall resistance using equa-

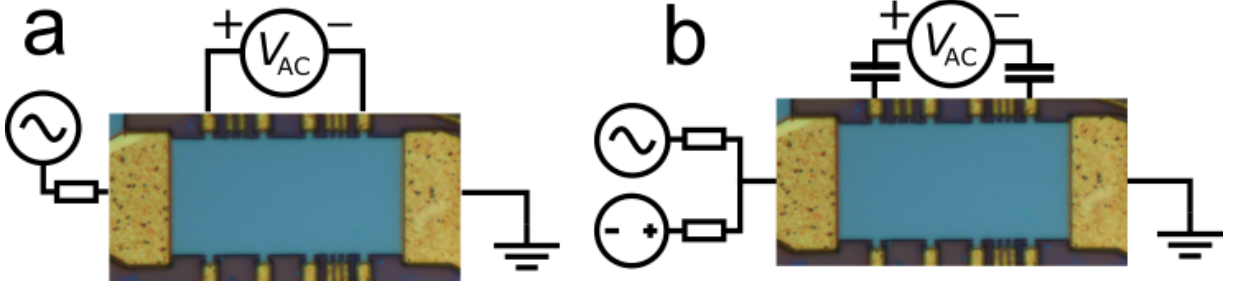


Figure 2.2: (a) The longitudinal resistance (R_{xx}) measurement configuration. (b) The differential resistance (dV/dI) measurement configuration, with AC coupling.

tion (1.15). Figure 2.3a shows the longitudinal resistance, R_{xx} , of the graphene measured as a function of gate voltage, V_G . Figure 2.3b shows the Hall resistance, $R_{xy} = R_{xy}(V_G)$. Here R_{xy} was symmetrised with respect to B , $R_{xy} = (R_{xy}(0.5T) - R_{xy}(-0.5T))/2$, to remove contributions from R_{xx} . The inset of Figure 2.3a shows the calculated conductivity $\sigma_{xx}(V_G) = 1/\rho_{xx} = W/R_{xx}L$ and the inset of Figure 2.3b shows the carrier density $n(V_G) = B/(eR_{xy})$. The sign of n changes and $\sigma_{xx} \rightarrow 0$ at $V_G \approx -0.5$ V which indicates a transition from holes to electrons across the charge neutrality point, at the tip of the Dirac cone. We also observe an asymmetry in σ_{xx} . The conductivity, σ_{xx} , is almost twice as large for hole conduction than for electron conduction at large $|V_G| \gtrsim 30$ V. This asymmetry is commonly observed in our graphene samples [47]. At high $V_G = \pm 60$ V, for both types of charge carrier, $\sigma_{xx} \sim 0.1\Omega^{-1}$ which implies $\mu = ne/\sigma_{xx} \sim 1 \times 10^6 \text{ cm}^2\text{V}^{-1}\text{s}^{-1}$. This indicates the graphene is exceptionally high quality as compared with others in the literature [48].

To further confirm the quality of the graphene we measured transverse magnetic focussing (TMF) across a large length $L = 20 \mu\text{m}$. Figure 2.4b shows the resistance $R = R(B, n)$ of the graphene measured in the TMF measurement configuration, as shown in Figure 2.4a. When the cyclotron radius, R_c , is such that the distance between current and voltage contacts $L = 2R_cp$, where p is an integer, ballistic charge carriers are focussed

onto the positive voltage contact. This gives rise to a peak in resistance $R \equiv V/I$. The peak positions were fitted to equation (1.21) with $L = 20.6 \pm 0.6 \mu\text{m}$. This is comparable with distance $L = 20 \mu\text{m}$ measured with optical microscopy. This result proves these peaks are due to magnetic focussing and suggests holes in our sample are not scattered significantly by defects in the bulk.

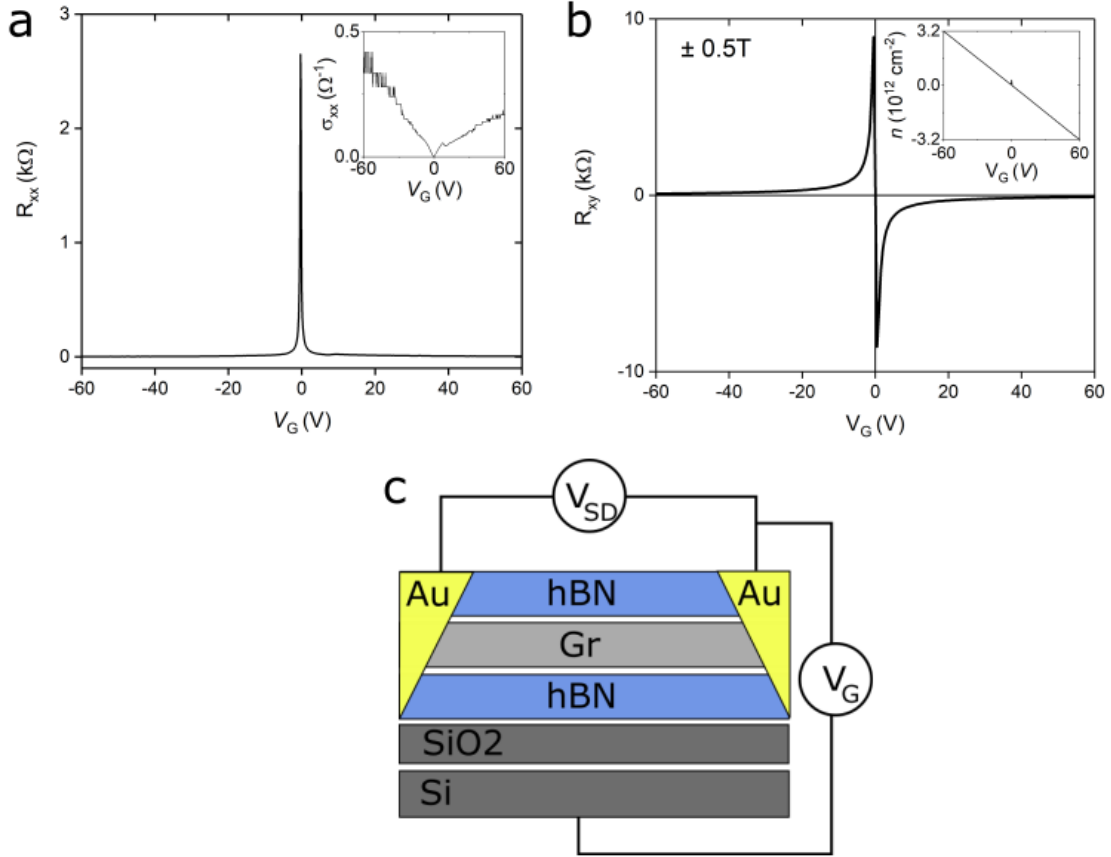


Figure 2.3: (a) R_{xx} of the graphene under test measured as a function of V_G at 5 K. (inset) $\sigma_{xx} = 1/\rho_{xx} = 1/(R_{xx}W/L) = \sigma_{xx}(V_G)$, where $W = 15 \mu\text{m}$ and $L = 20 \mu\text{m}$. (b) R_{xy} as a function of V_G at 5K, symmetrised with respect to B ; i.e., $R_{xy} = (R_{xy}(0.5T) - R_{xy}(-0.5T))/2$. (inset) $\sigma_{xy} = 1/R_{xy}^{asym} = \sigma_{xy}(V_G)$. (c) Cross-section of the device under test. hBN-encapsulated graphene is situated on SiO_2 on Si. Source-drain voltage, V_{SD} , is applied across one dimensional gold contacts. A gate voltage, V_G , is applied across one of the gold contacts and the Si/SiO₂/hBN layers.

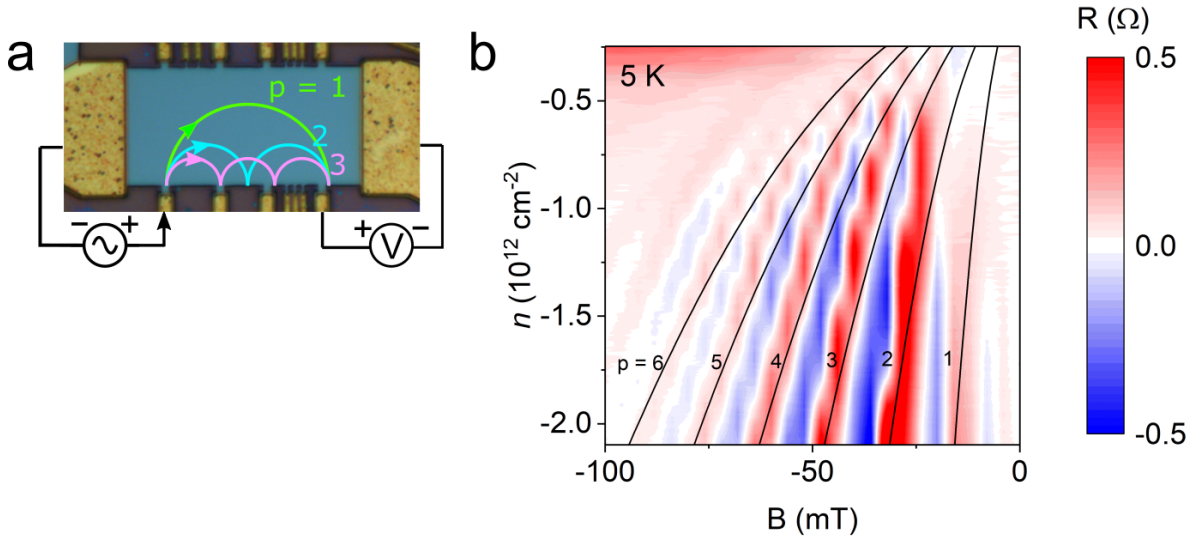


Figure 2.4: (a) A schematic diagram of the TMF configuration with an optical micrograph image of the graphene Hall bar under test. Three magnetic focussing trajectories are shown with $L = 2R_{cp}$ for $p = 1, 2, \text{ and } 3$, in green, cyan and pink, respectively. (b) Magnetoresistance, $R = R(B, n)$, of the graphene in the TMF measurement configuration, shown in (a), at 5 K. Solid curves are described by equation (1.21) with $L = 20.6 \mu\text{m}$ and $p = 1, 2, 3, 4, 5 \text{ and } 6$, respectively.

Chapter 3

Magnetic Focussing in Wide Graphene Hall Bars

This section discusses my contribution to our recent paper [11] (supplementary Section 2) reporting the first observation of magnetophonon oscillations in graphene. In our widest samples, where the width is greater than the distance between the current and positive voltage probe, we observed magnetic focussing peaks embedded in the magnetophonon oscillations. These magnetic focussing peaks had an unexpected phase shift when fitted to equation (1.21). The work presented in this chapter confirms the origin of the magnetic focussing peaks and shows how this phase shift follows from the longitudinal resistance measurement configuration.

Figure 3.1b shows the longitudinal resistance, $R_{xx} = R_{xx}(B, n)$, of the Hall bar shown in Figure 3.1a, with low $B < 0.2$ T, at 5 K. We observe peaks in R_{xx} , labelled $p = 1/2, 3/2$ and $5/2$, respectively. These peaks are attributed to magnetic focussing; i.e., the resistance $R_{xx} = V_{xx}/I$ is maximal when ballistic charge carriers are focussed a distance $L = 2R_c p$ by the magnetic field B . The peak labelled $p = 1/2$ is at a field $B_{p=1/2}$. This corresponds to a significant phase shift. The peak positions were fitted to equation (1.21) with $L = (6.0 \pm 0.1)$ μm and $p = 1/2, 3/2$ and $5/2$, respectively. The magnetic field B was offset by 3.5 mT to symmetrise R_{xx} with respect to B . This offset is justified from the symmetry of the measurement configuration and is likely due to trapped

magnetic field. The measured value of $L = (6.0 \pm 0.1) \mu\text{m}$ is close to the distance $L \approx 5 \mu\text{m}$ measured with an optical microscope, thus proving the peaks are due to magnetic focussing.

To explain the half integer shift from integer p we first note that carriers can be injected from anywhere on the contact. For the magnetic focussing process the injection point can be restricted however, since carriers injected at a distance $d_c > 2R_c$ from the channel edge are focussed back into the injector. In magnetic focussing, charge carriers must therefore have been injected at a distance $d_c < 2R_c$ from the channel edge. Each injection point along this line has a different shift in p relative to equation (1.21). Injection at the bottom corner gives rise to semicircular skipping orbits as shown figure 2.4, which are described precisely by equation (1.21) with integer p . Injection halfway between this line segment gives rise to a shift $p \rightarrow p - 1/2$, which corresponds to a quarter circle trajectory before the first reflection and a continuation on semicircular trajectories between subsequent reflections. In this picture injected carriers are collimated perpendicular to the contact surface. This can be explained by the tunnelling of Dirac fermions through a p-n junction formed at the contact interface [49], and has previously been demonstrated in graphene [50].

We have thus proved the origin of the magnetic focussing over a distance $L \approx 5 \mu\text{m}$ and explained the unexpected phase shift as a natural consequence of parallel injection in the longitudinal measurement configuration. We have also therefore shown that carriers are propagating along the edge of the channel at the Fermi velocity. This presents a potential problem because the characteristic frequency of skipping orbits, $f_{skip} = 1/\tau_{skip} = v_F/2R_c$, is greater than the characteristic frequency of MPR, $f_{MPR} = 1/\tau_{MPR} = v_{MPR}/2R_c$, where v_{MPR} is the drift velocity associated with MPR scattering [11]. This suggests magnetic focussing should dominate MPR. In our wide graphene Hall bar however, MPR oscillations are prominent, because many MPR orbits fit into the bulk of width $W > 2R_c$, in contrast

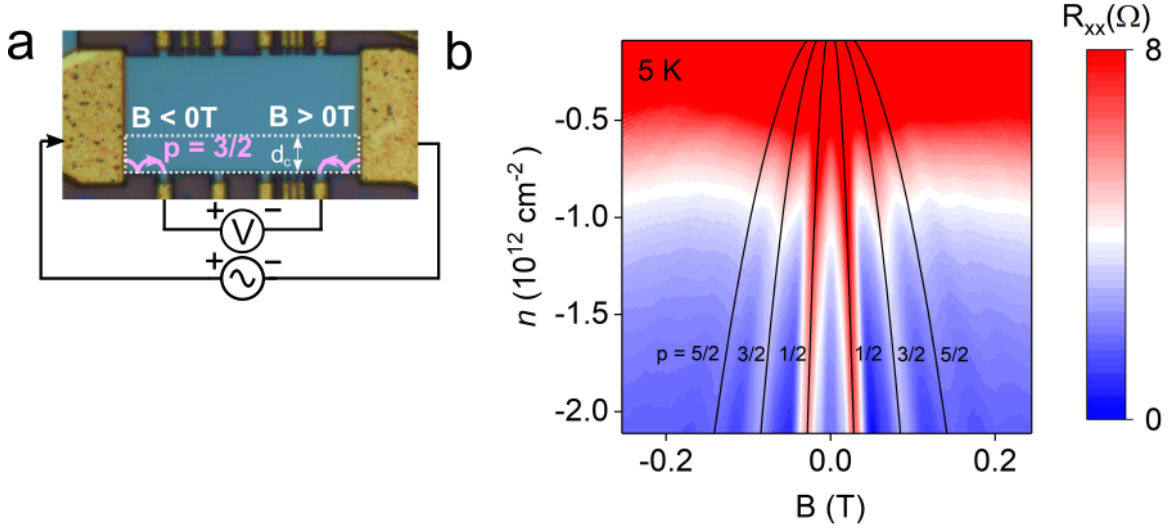


Figure 3.1: (a) A schematic diagram of a longitudinal resistance (R_{xx}) measurement configuration with an optical micrograph image of the graphene Hall bar under test. Two magnetic focussing trajectories (pink) are shown spanning a distance $L = 2R_c p$ with $p = 3/2$, for $B < 0$ T and $B > 0$ T, respectively. The white boundary shows all points at a distance $d_c < 2R_c$ from the channel edge. Carriers injected outside this region are focussed back into the contact. (b) $R_{xx} = R_{xx}(B, n)$ of the graphene in the measurement configuration shown in (a), at 5 K. Solid curves depict the function described by equation (1.21) with a fitting parameter $L = 6.0 \mu\text{m}$ and $p = 1/2, 3/2$ and $5/2$. These curves are offset by $B_p = -3.5\text{mT}$ to symmetrise the peak positions with respect to B .

to magnetic focussing trajectories, which are confined to a distance $d_c < R_c$ from the channel edge.

Chapter 4

Magnetophonon Oscillations in Graphene with a Large DC Bias

This chapter reports on MPR with large direct currents (up to 1 mA) passing through the graphene Hall bar. Previous measurements of MPR oscillations in graphene were performed at low currents and thus low electric fields [11]. Here we use a large current to generate large electric fields in order to heat the charge carriers out of equilibrium with phonons in the lattice, so that more phonons are emitted than absorbed. We observed the MPR oscillations are split at a sufficiently large direct current due to a Hall-field induced Landau level tilting. At $I_{DC} \approx 1$ mA we also observe maxima in the differential resistance as the carrier drift velocity approaches the speed of the TA phonon ($v_s = 13$ kms⁻¹). Finally, we observed the fundamental ($q = 1$) Hall-induced resistance oscillation (HIRO) arise when the Landau level states align in energy. We study this oscillation as a function carrier density and show the amplitude is increased at low n . This observation is consistent with the idea that HIRO is due to scattering off impurities in the lattice [28].

Figure 4.1a shows a greyscale map of the differential magnetoresistance, $dV/dI = r_{xx} = r_{xx}(I_{DC}, B)$, with a hole carrier density $n = 3.2 \times 10^{16}$ cm⁻², at $T = 40$ K. At $B < 0.2$ T we observe peaks which appear independent of I_{DC} . These are the magnetic focussing peaks discussed in the previous chapter. Other peaks in dV/dI are marked by coloured squares. Blue, red, and green squares represent MPR peak positions with $p = 1, 2,$ and 3 ,

respectfully. The squares at $I_{DC} = 0 \mu\text{A}$ are obtained from the MPR oscillations in our recent paper [11]. These peaks split into two with increasing I_{DC} . The splitting of the blue $p = 1$ peak is shown in Figure 4.1b and Figure 4.1c. Local maxima arise where the peaks intersect with split peaks of different p . This peak splitting is attributed to a Hall field-induced spatial tilting of the Landau levels, which modifies the energies of the $q = 2\hbar k_F$ MPR transitions. These peaks were fit to equation (1.33) with $v_F = (1.06 \pm 0.04) \times 10^6 \text{ kms}^{-1}$ for $p = 1$ (blue), $p = 2$ (red), and $p = 3$ (green). This is consistent with the measured $v_F = (1.06 \pm 0.05) \times 10^6 \text{ ms}^{-1}$ obtained from the temperature dependence of the SdH oscillations [11]. This result proves the MPR oscillations are splitting due to Hall-field induced Landau level tilting.

At higher $I_{DC} \approx 1000 \mu\text{A}$ we observe a small peak as the drift velocity $v_d = j/ne$ approaches the velocity of the TA phonon ($v_s \approx 13 \text{ kms}^{-1}$). These are marked by pink squares. We attribute this peak to additional carrier-phonon scattering when the Landau levels become parallel to the phonon dispersion. This new scattering channel arises because the number of phonons satisfying energy-momentum conservation increases. The effect was previously seen in conventional semiconductors by Zhang et al [29]. Interestingly, the peak in our data is accompanied by an apparent shift of the magnetic focussing peaks (at $I_{DC} \gtrsim 800 \mu\text{A}$). This could be explained by diffusive scattering of the collimated electron beam as v_d approaches v_s . Further work is required to test this hypothesis.

Figure 4.2 shows the Hall voltage $V_{xy} = V_{xy}(I_{DC})$ with $B = 0.8 \text{ T}$, at 40 K (red) and 5 K (blue) respectively. This was calculated by integrating the differential Hall resistance, dV_{xy}/dI , with respect to I_{DC} . Red V_{xy} data was measured simultaneously with $r_{xx}(I_{DC}, B = 0.8\text{T})$ in Figure 4.1 and blue V_{xy} data was measured simultaneously with $r_{xx}(I_{DC}, B = 0.8\text{T})$ in Figure 4.3. The carrier density $n = (3.25 \pm 0.01) \times 10^{12} \text{ cm}^{-2}$ was measured by fitting the blue V_{xy} data to $V_{xy} = I_{DC}R_{xy} = I_{DC}B/ne$. This is comparable with $n = 3.2 \times 10^{12} \text{ cm}^{-2}$ measured at low AC bias ($I_{AC} \approx 1 \mu\text{A}$) in our recent paper [11].

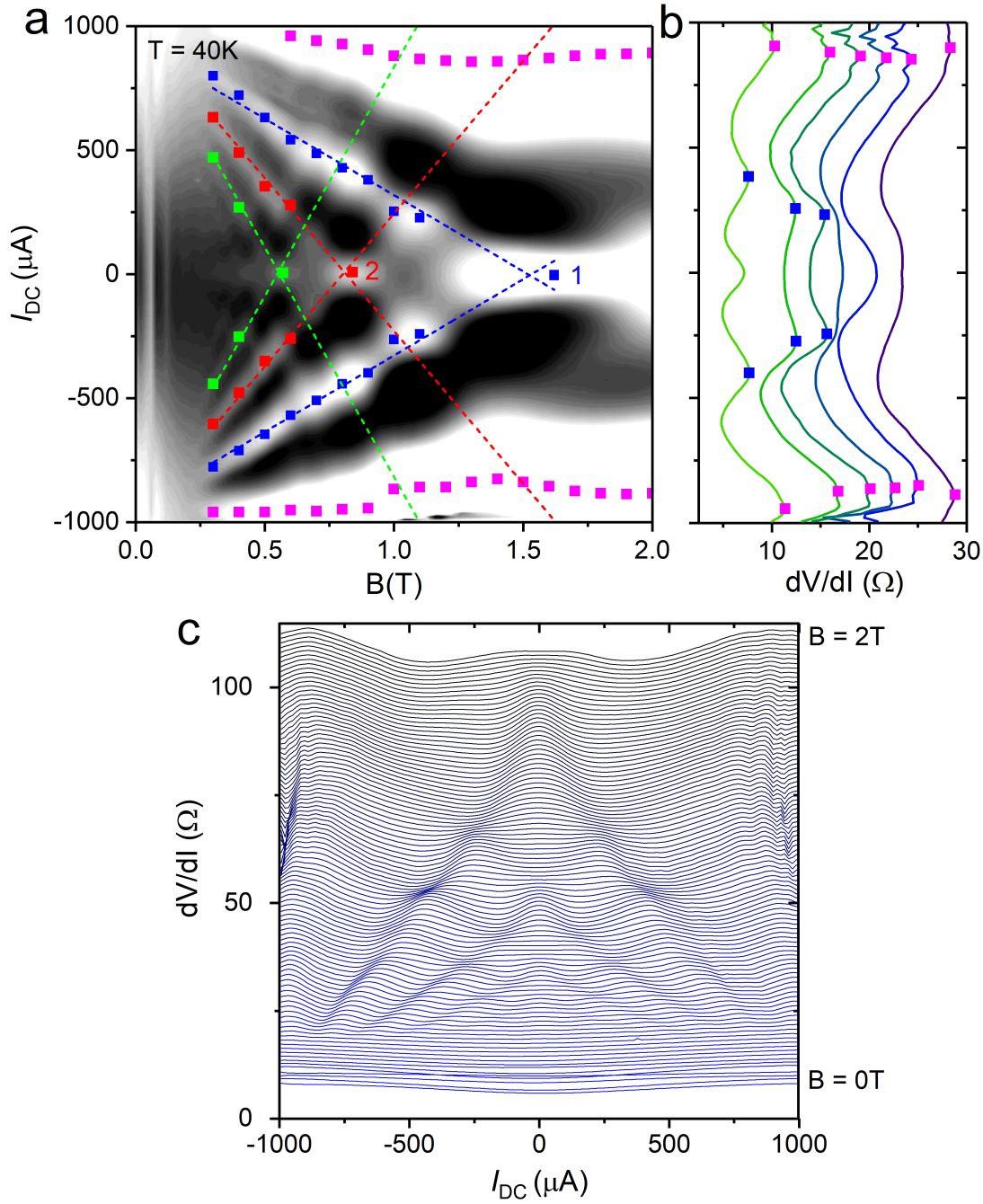


Figure 4.1: (a) $dV/dI = r_{xx} = r_{xx}(I_{DC}, B)$ at 40 K from $B = 0\text{ T}$ to $B = 2\text{ T}$ at intervals $\Delta B = 0.02\text{ T}$; from $10\ \Omega$ (black) to $16\ \Omega$ (white). Blue, red, and green squares mark the position of the $p = 1, 2$ and 3 MPR peaks respectively. Lines of the same colour show a fit of these peak positions to equation (1.33) with $v_F = 1.06 \times 10^6\ \text{ms}^{-1}$. (b) Waterfall plot of the data from (a) from $B = 1.1\text{ T}$ to $B = 1.5\text{ T}$ at intervals $\Delta B = 0.1\text{ T}$, and then $B = 2.0\text{ T}$. Curves are offset for clarity. (c) Full waterfall plot of the data in Figure 4.1a. Curves are offset in intervals of $2\ \Omega$.

The inset shows $r_{xy} = dV_{xy}/dI$ measured as a function of I_{DC} . Black lines show the fitted $R_{xy} = B/ne$ with $n = (3.25 \pm 0.01) \times 10^{12} \text{ cm}^{-2}$. The differential Hall resistance, dV_{xy}/dI , does not deviate significantly from the Hall resistance, $R_{xy} = V_{xy}/I$, which suggests the MPR peaks are not shifting due to changes in n .

Figure 4.3a shows $dV/dI = r_{xx}(I_{DC}, B)$ with a hole carrier density $n = 3.2 \times 10^{12} \text{ cm}^{-2}$, at 5 K. Magnetic focussing oscillations are observed at $B < 0.2 \text{ T}$, as before. At $I_{DC} \sim 10 \mu\text{A}$ we observe SdH oscillations. These fade at $I_{DC} \gtrsim 50 \mu\text{A}$ and split MPR oscillations emerge at $I_{DC} \gtrsim 100 \mu\text{A}$. The carrier density $n = (3.32 \pm 0.03) \times 10^{12} \text{ cm}^{-2}$ was calculated from the period of the SdH oscillations. This is in close agreement with $n = (3.25 \pm 0.01) \times 10^{12} \text{ cm}^{-2}$ measured from the Hall resistance. The lines from Figure 4.1a are drawn on Figure 4.3a to confirm the origin of the split MPR peaks. The split MPR peaks are aligned with these lines, albeit with a small offset. This offset could be attributed to an energy shift in the resonance condition. Further work is needed to clarify these effects.

At lower $B \lesssim 0.5 \text{ T}$ a new peak, marked by cyan triangles, emerges from $B = 0 \text{ T}$ with a position proportional to I_{DC} , which intersects with the split MPR peaks. We attribute this peak to Hall field-induced inter Landau-Level scattering. The cyan triangles were fitted to equation (1.35) with $v_F = (1.05 \pm 0.01) \times 10^6 \text{ ms}^{-1}$ and $q = 1$. This is consistent with $v_F = (1.06 \pm 0.05) \times 10^6 \text{ ms}^{-1}$ measured from the temperature dependence of the SdH oscillations [11]. At higher I_{DC} , a weak oscillation, described by equation (1.35) with $q = 2$ and $v_F = (1.06 \pm 0.05) \times 10^6 \text{ ms}^{-1}$, is also observed. These HIRO have never before been observed in graphene. Our observations also demonstrate a more accurate and far less labour intensive measure of v_F than the SdH oscillation method used in our recent publication [11]. This was the most significant source of error in the measured TA phonon velocity $v_s = 13.6 \pm 0.7 \text{ kms}^{-1}$.

In Figure 4.4 we show $dV/dI = r_{xx}(B)$ at $I_{DC} = 250 \mu\text{A}$ and 5 K, at different

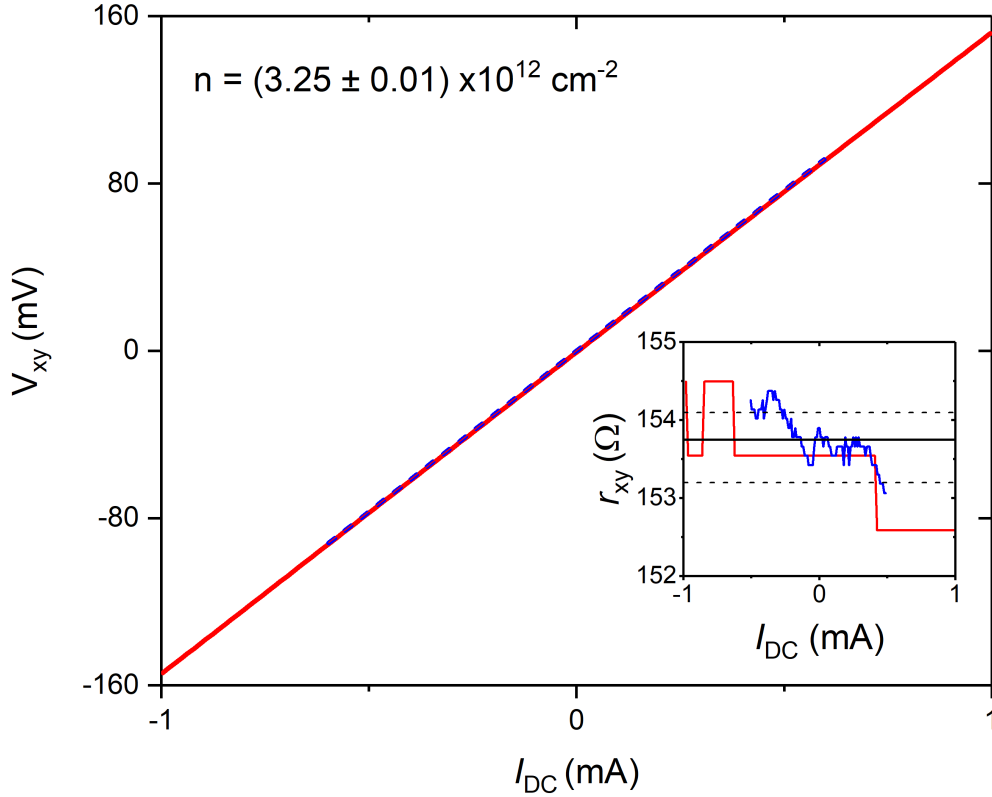


Figure 4.2: Hall voltage, V_{xy} , as a function of I_{DC} at $B = 0.8 \text{ T}$, measured at the same time as $dV/dI = r_{xx} = r_{xx}(0.8 \text{ T})$ at 5 K (blue) and 40 K (red). (inset) Differential Hall resistance, $dV_{xy}/dI = r_{xy}$, as a function of I_{DC} , measured at the same time as $r_{xx} = r_{xx}(0.8 \text{ T})$ at 5 K (blue) and 40 K (red). The black lines show $R_{xy} = -B/ne$ with $n = 3.25 \pm 0.01 \times 10^{12} \text{ cm}^{-2}$. The differential Hall resistance, r_{xy} , does not deviate significantly from these lines which suggests n is constant over this range of I_{DC} .

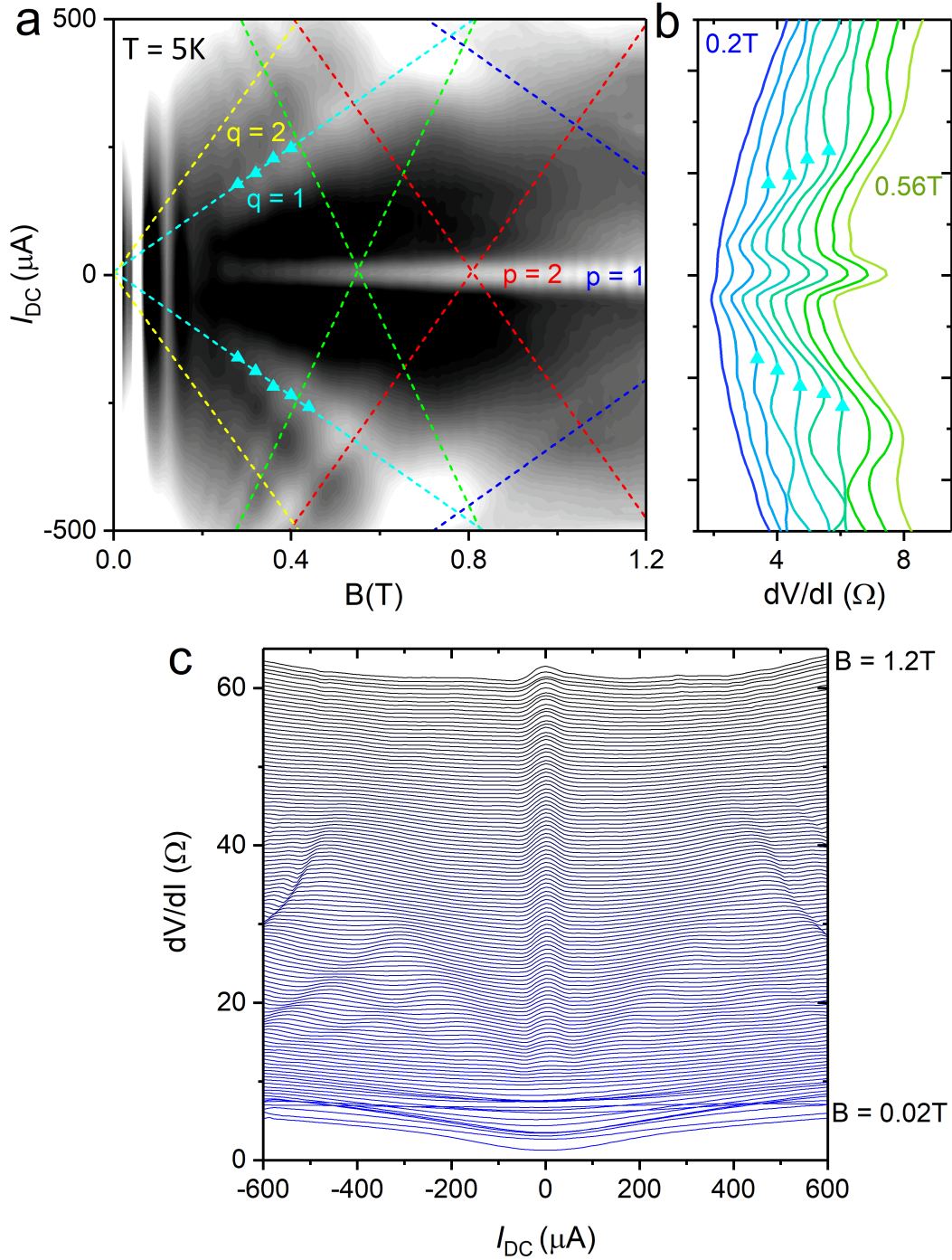


Figure 4.3: (a) $dV/dI = r_{xx} = r_{xx}(I_{DC}, B)$ at 5 K from $B = 0.02\text{ T}$ to $B = 1.2\text{ T}$, at intervals $\Delta B = 0.01\text{ T}$; ranging from $1.4\text{ }\Omega$ (black) to $3.6\text{ }\Omega$ (white). Solid lines from Figure 4.1 are also shown. Cyan triangles mark the position of the $q = 1$ HIRO peak and the cyan dotted line shows a fit of these to equation (1.35) with $v_F = 1.05 \times 10^6 \text{ ms}^{-1}$ and $q = 1$. Yellow dotted lines show the lines described by equation (1.35) with $q = 2$ and the same v_F . (b) Traces from (a) from $B = 0.16\text{ T}$ to 0.56 T at intervals $\Delta B = 0.04\text{ T}$. Curves are offset for clarity (c) Full waterfall plot of the data in (a). The curves are offset in intervals of $0.5\text{ }\Omega$.

carrier densities, n . These curves were obtained by sweeping B at fixed $I_{DC} = 250 \mu\text{A}$, in contrast to previous measurements where B is fixed and I_{DC} is swept. At $B \lesssim 0.2 \text{ T}$ we observe the magnetic focussing peaks, as before. At $B \approx \pm 0.41 \text{ T}$ we observe a pronounced maxima in dV/dI for all measured carrier densities. We speculate that this maxima could be the fundamental ($q = 1$) HIRO. Figure 4.5 shows the peak positions from Figure 4.4 together with the lines described by the $p = 1$ HIRO and split MPR oscillations. Error bars are estimated from those expected after a subtraction of the background. Blue lines depict HIRO, described by equation (1.35), with $v_F = (1.05 \pm 0.01) \times 10^6 \text{ ms}^{-1}$ and $p = 1$; green, red, and purple lines depict split MPR, described by equation (1.33) with $v_F = (1.05 \pm 0.01) \times 10^6 \text{ ms}^{-1}$ and $v_s = 13.7 \pm 0.7 \text{ kms}^{-1}$ for $p = 1, 2$ and 3 , respectively. Apart from the peak at $n = 1.5 \times 10^{12} \text{ cm}^{-2}$, the lines describing the split MPR peaks do not intersect the peaks at $B = \pm 0.41 \text{ T}$. This suggests the peaks are due to HIRO. In addition, as shown in Figure 4.4, the amplitude of this HIRO is larger at lower n . We speculate that this could be due to a decreased carrier screening of impurities providing the $2\hbar k_F$ momentum transfer in the bulk.

In this chapter we have observed three distinct processes when a wide graphene Hall bar is subject to strong electric fields. At sufficiently large Hall electric field, we discovered a splitting of the MPR oscillations due to a spatial tilting of the Landau levels, which modifies the energies of $2\hbar k_F$ transitions. At large $I_{DC} \approx 1 \text{ mA}$, when the drift velocity approaches the speed of the TA phonon ($v_s \approx 13 \text{ kms}^{-1}$), we observed a maxima emerge when the Landau levels become parallel to the phonon dispersion. Finally, we observed the fundamental ($q = 1$) HIRO arise when the Landau level states become aligned in energy at $q = 2\hbar k_F$. This demonstrates a useful method for finding v_F by means of magnetotransport studies. Finally, our measurements as a function of n suggest the HIRO amplitude is larger at lower n . We speculated that this might be due to a decreased screening of scatterers at low n .

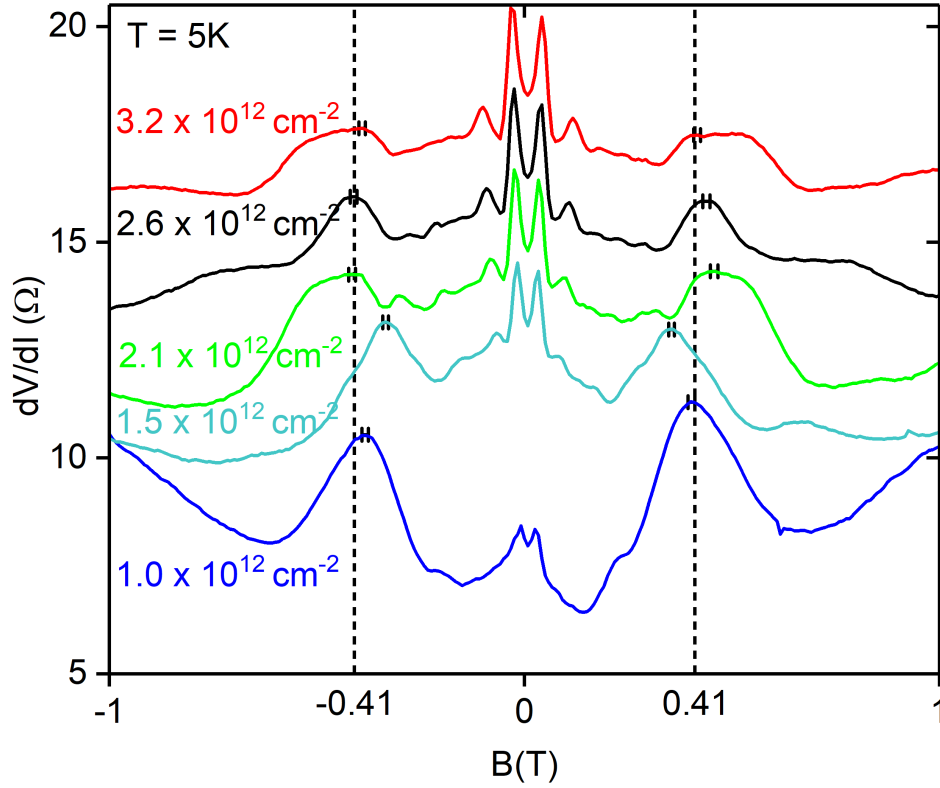


Figure 4.4: Plot of $dV/dI = r_{xx} = r_{xx}(B, n)$ at $I_{DC} = -250 \mu\text{A}$, from a hole carrier density $n = 1 \times 10^{12} \text{ cm}^{-2}$ to $n = 3.2 \times 10^{12} \text{ cm}^{-2}$ at intervals $\Delta n = 0.6 \times 10^{12} \text{ cm}^{-2}$, at 5 K. Dotted lines show the position of the $p = 1$ HIRI at $B = \pm 0.41 \text{ T}$. The curves are offset for clarity.

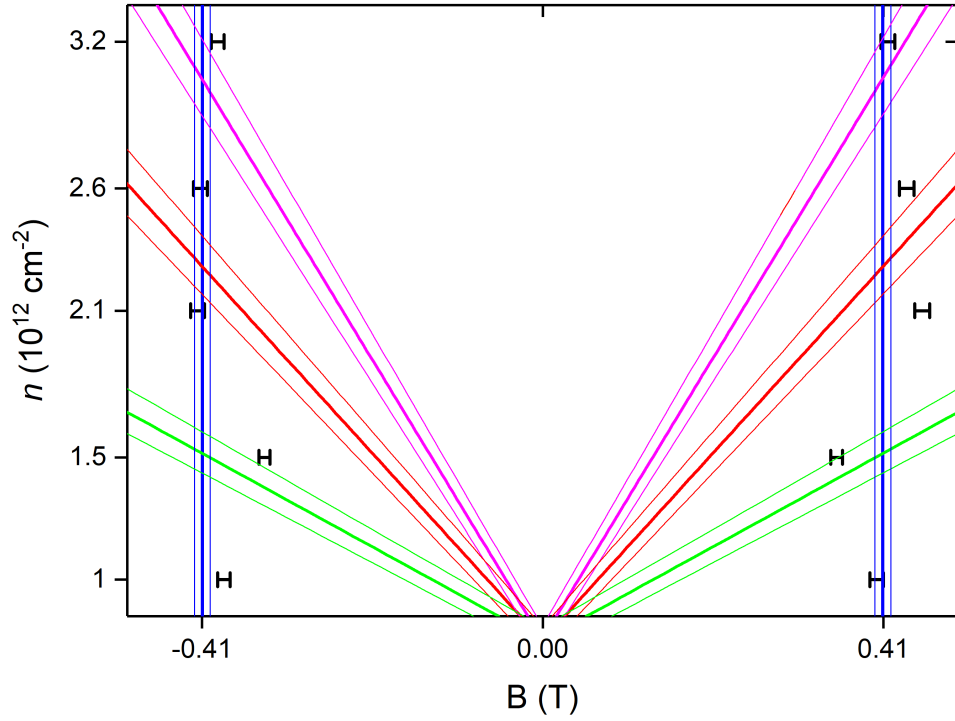


Figure 4.5: Peak positions from figure 4.4 plotted with the lines described by HIRO and split MPR. The blue lines are described by equation (1.35) for HIRO with $v_F = (1.05 \pm 0.01) \times 10^6 \text{ ms}^{-1}$. The green, red and pink lines are described by equation (1.33) for split MPR with $v_s = 13.7 \pm 0.7 \text{ kms}^{-1}$ and $v_F = (1.05 \pm 0.01) \times 10^6 \text{ ms}^{-1}$, with $p = 1, 2$ and 3 , respectively.

Chapter 5

Conclusion and Outlook

This thesis reports on magnetophonon oscillations in graphene. These oscillations have previously been used to demonstrate, for the first time, that TA phonons (rather than LA phonons) limit the temperature-dependent resistivity in graphene [11]. In this thesis we prove that carriers are simultaneously skipping along the edge of the graphene channel at the Fermi velocity. This gives rise to magnetic focussing peaks at low $B \lesssim 0.2\text{T}$, when the distance between the current and voltage contacts $L = 2R_c p$, where p is an integer. We attributed a phase shift of these peaks to a shift $p \rightarrow p - 1/2$, due to collimated injection in the longitudinal measurement configuration. We also studied MPR oscillations with large currents and thus large electric fields. We demonstrated a splitting of the MPR oscillations due to a spatial tilting of the Landau levels in a strong Hall electric field. This tunes the energy of the MPR transitions and thus allows access to lower energy modes in the TA phonon dispersion. At larger $I_{DC} \sim 1\text{ mA}$, we also discovered additional differential resistance maxima arising when the drift velocity approaches the speed of the TA phonon; i.e., when Landau level states become parallel to the TA phonon dispersion. Finally, we observed the fundamental ($p = 1$) HIRO arising when the Landau level states are aligned in energy at $q \approx 2\hbar k_F$. This provides a far less labour intensive measure of v_F as compared with the standard method of measuring the amplitude of SdH oscillations. We studied the amplitude this peak over a range of carrier densities and observed the peak amplitude is largest at lower n . We speculated that this could be due to a decreased screening of

impurities at low n .

Our next step would be to use MPR oscillations to measure other types of phonon in graphene heterostructures. We could use MPR oscillations (tuned by the Hall-electric field) to see if these phonons are relevant for carrier scattering. For example, interlayer breathing modes are thought to flatten the ZA phonon dispersion at low energies (~ 100 meV), leading to a large phonon density of states [51], which might give rise to significant phonon scattering. We could also look for MPR oscillations due to intervalley scattering by higher energy phonons, including optical phonons, as suggested by Mori and Ando [42]. Another possibility could be to use MPR oscillations to measure the low-energy phonon dispersion in twisted bilayer graphene. A better understanding of electron-phonon interactions in this material could improve our understanding of the superconductivity mechanism in twisted bilayer graphene [9, 10].

Bibliography

- [1] Wallace PR. The Band Theory of Graphite. *Physical Review*. 1947 may;71(9):622–634. Available from: <https://link.aps.org/doi/10.1103/PhysRev.71.622>.
- [2] Novoselov KS, Geim AK, Morozov SV, Jiang D, Katsnelson MI, Grigorieva IV, et al. Two-dimensional gas of massless Dirac fermions in graphene. *Nature*. 2005;438(7065):197–200. Available from: <https://doi.org/10.1038/nature04233>.
- [3] Zhang Y, Tan YW, Stormer HL, Kim P. Experimental observation of the quantum Hall effect and Berry's phase in graphene. *Nature*. 2005;438(7065):201–204. Available from: <https://doi.org/10.1038/nature04235>.
- [4] Castro Neto AH, Guinea F, Peres NMR, Novoselov KS, Geim AK. The electronic properties of graphene. *Reviews of Modern Physics*. 2009 jan;81(1):109–162. Available from: <https://link.aps.org/doi/10.1103/RevModPhys.81.109>.
- [5] Novoselov KS, Geim AK, Morozov SV, Jiang D, Zhang Y, Dubonos SV, et al. Electric field in atomically thin carbon films. *Science*. 2004 oct;306(5696):666–669. Available from: <http://science.sciencemag.org/content/306/5696/666.abstract>.
- [6] Young AF, Kim P. Quantum interference and Klein tunnelling in graphene heterojunctions. *Nature Physics*. 2009 feb;5:222–226. Available from: <https://doi.org/10.1038/nphys1198><http://10.0.4.14/nphys1198><https://www.nature.com/articles/nphys1198#supplementary-information>.
- [7] Geim AK, Grigorieva IV. Van der Waals heterostructures. *Nature*. 2013 jul;499:419–425. Available from: <https://doi.org/10.1038/nature12385><http://10.0.4.14/nature12385>.
- [8] Cao Y, Fatemi V, Fang S, Watanabe K, Taniguchi T, Kaxiras E, et al. Unconventional superconductivity in magic-angle graphene superlattices. *Nature*. 2018 mar;556(7699):43–50. Available from: <https://www.nature.com/articles/nature26160#supplementary-information>.
- [9] Wu F, Macdonald AH, Martin I. Theory of Phonon-Mediated Superconductivity in Twisted Bilayer Graphene. *Physical Review Letters*. 2018 dec;121(25):257001. Available from: <https://link.aps.org/doi/10.1103/PhysRevLett.121.257001>.
- [10] Koshino M, Son YW. Moiré phonons in the twisted bilayer graphene. *Physical Review B*. 2019 aug;100(7):075416. Available from: <https://ui.adsabs.harvard.edu/abs/2019arXiv190509660K>.

- [11] Kumaravadivel P, Greenaway MT, Perello D, Berdyugin A, Birkbeck J, Wengraf J, et al. Strong magnetophonon oscillations in extra-large graphene. *Nature Communications*. 2019;10(1):3334. Available from: <https://doi.org/10.1038/s41467-019-11379-3>.
- [12] Kossacki P, Faugeras C, Kühne M, Orlita M, Mahmood A, Dujardin E, et al. Circular dichroism of magnetophonon resonance in doped graphene. *Physical Review B - Condensed Matter and Materials Physics*. 2012;86(20):205431.
- [13] Kim Y, Poumirol JM, Lombardo A, Kalugin NG, Georgiou T, Kim YJ, et al. Measurement of filling-factor-dependent magnetophonon resonances in graphene using Raman spectroscopy. *Physical Review Letters*. 2013 may;110(22):227402. Available from: <https://link.aps.org/doi/10.1103/PhysRevLett.110.227402>.
- [14] Mohr M, Maultzsch J, Dobardžić E, Reich S, Milošević I, Damnjanović M, et al. Phonon dispersion of graphite by inelastic x-ray scattering. *Physical Review B*. 2007 jul;76(3):035439. Available from: <https://link.aps.org/doi/10.1103/PhysRevB.76.035439>.
- [15] Greenaway MT, Krishna Kumar R, Kumaravadivel P, Geim AK, Eaves L. Magnetophonon spectroscopy of Dirac Fermion scattering by transverse and longitudinal acoustic phonons in graphene. *Physical Review B (in press)*. 2019; Available from: <https://ui.adsabs.harvard.edu/abs/2019arXiv190503602G>.
- [16] Katsnelson MI. *Graphene: carbon in two dimensions*. Cambridge University Press; 2012.
- [17] Elias DC, Gorbachev RV, Mayorov AS, Morozov SV, Zhukov AA, Blake P, et al. Dirac cones reshaped by interaction effects in suspended graphene. *Nature Physics*. 2011 jul;7(9):701–704. Available from: <http://www.nature.com/doi/10.1038/nphys2049>.
- [18] Ashcroft NW, Mermin ND. *Solid State Physics*. Harcourt; 1976.
- [19] Beenakker CWJ. Colloquium: Andreev reflection and Klein tunneling in graphene. *Reviews of Modern Physics*. 2008 oct;80(4):1337–1354. Available from: <https://link.aps.org/doi/10.1103/RevModPhys.80.1337>.
- [20] Kittel C. *Introduction to solid state physics*. vol. 8. 8th ed. New York: Wiley; 2005.
- [21] Simon SH. *The Oxford solid state basics*. Oxford University Press; 2013.
- [22] van Houten H, Beenakker CWJ, Williamson JG, Broekaart MEI, van Loosdrecht PHM, van Wees BJ, et al. Coherent electron focusing with quantum point contacts in a two-dimensional electron gas. *Physical Review B*. 1989 apr;39(12):8556–8575. Available from: <https://link.aps.org/doi/10.1103/PhysRevB.39.8556>.

- [23] Mayorov AS, Gorbachev RV, Morozov SV, Britnell L, Jalil R, Ponomarenko LA, et al. Micrometer-Scale Ballistic Transport in Encapsulated Graphene at Room Temperature. *Nano Letters*. 2011 jun;11(6):2396–2399. Available from: <https://doi.org/10.1021/nl200758b>.
- [24] Taychatanapat T, Watanabe K, Taniguchi T, Jarillo-Herrero P. Electrically tunable transverse magnetic focusing in graphene. *Nature Physics*. 2013 feb;9(4):225–229. Available from: <http://www.nature.com/doi/10.1038/nphys2549>.
- [25] Ariel V, Natan A. Electron effective mass in graphene. In: 2013 International Conference on Electromagnetics in Advanced Applications (ICEAA); 2013. p. 696–698.
- [26] Karssemeijer LJ, Fasolino A. Phonons of graphene and graphitic materials derived from the empirical potential LCBOPII. *Surface Science*. 2011;605(17-18):1611–1615. Available from: <http://www.sciencedirect.com/science/article/pii/S0039602810004437>.
- [27] Stradling RA. The magnetophonon effect. *Journal of Physics E: Scientific Instruments*. 1972;5(8):736–740. Available from: <http://www.sciencedirect.com/science/article/pii/0079672785900047>.
- [28] Dmitriev IA, Mirlin AD, Polyakov DG, Zudov MA. Nonequilibrium phenomena in high Landau levels. *Reviews of Modern Physics*. 2012;84(4):1709–1763.
- [29] Zhang W, Zudov MA, Pfeiffer LN, West KW. Resonant phonon scattering in quantum hall systems driven by dc electric fields. *Physical Review Letters*. 2008 jan;100(3):36805. Available from: <https://link.aps.org/doi/10.1103/PhysRevLett.100.036805>.
- [30] Zudov MA, Du RR, Simmons JA, Reno JL. Shubnikov-de Haas-like oscillations in millimeterwave photoconductivity in a high-mobility two-dimensional electron gas. *Physical Review B - Condensed Matter and Materials Physics*. 2001;64(20):201311.
- [31] Hwang EH, Das Sarma S. Screening-induced temperature-dependent transport in two-dimensional graphene. *Physical Review B - Condensed Matter and Materials Physics*. 2009 apr;79(16):165404. Available from: <https://link.aps.org/doi/10.1103/PhysRevB.79.165404>.
- [32] Zudov MA, Ponomarev IV, Efros AL, Du RR, Simmons JA, Reno JL. New Class of Magnetoresistance Oscillations: Interaction of a Two-Dimensional Electron Gas with Leaky Interface Phonons. *Physical Review Letters*. 2001 apr;86(16):3614–3617. Available from: <https://link.aps.org/doi/10.1103/PhysRevLett.86.3614>.
- [33] Eaves L, Hoult RA, Stradling RA, Tidey RJ, Portal JC, Askenazy S. Fourier analysis of magnetophonon and two-dimensional Shubnikov-de Haas magnetoresistance structure. *Journal of Physics C: Solid State Physics*. 1975;8(7):1034–1053. Available from: <http://dx.doi.org/10.1088/0022-3719/8/7/019>.

- [34] Tsui DC, Englert T, Cho AY, Gossard AC. Observation of Magnetophonon Resonances in a Two-Dimensional Electronic System. *Physical Review Letters*. 1980 feb;44(5):341–344. Available from: <https://link.aps.org/doi/10.1103/PhysRevLett.44.341>.
- [35] Bykov AA, Goran AV. Temperature dependence of magnetophonon resistance oscillations in GaAs/AlAs heterostructures at high filling factors. *JETP Letters*. 2009;90(8):578–581. Available from: <https://doi.org/10.1134/S0021364009200065>.
- [36] Hatke AT, Zudov MA, Pfeiffer LN, West KW. Phonon-induced resistance oscillations in 2D systems with a very high electron mobility. *Physical Review Letters*. 2009;102(8):86808.
- [37] Zhang W, Chiang HS, Zudov MA, Pfeiffer LN, West KW. Magnetotransport in a two-dimensional electron system in dc electric fields. *Physical Review B - Condensed Matter and Materials Physics*. 2007;75(4):41304(R).
- [38] Zudov MA, Dmitriev IA, Friess B, Shi Q, Umansky V, Von Klitzing K, et al. Hall field-induced resistance oscillations in a tunable-density GaAs quantum well. *Physical Review B*. 2017 sep;96(12):121301. Available from: <https://link.aps.org/doi/10.1103/PhysRevB.96.121301>.
- [39] Shi Q, Ebner QA, Zudov MA. Hall field-induced resistance oscillations in a p-type Ge/SiGe quantum well. *Physical Review B - Condensed Matter and Materials Physics*. 2014 oct;90(16):161301. Available from: <https://link.aps.org/doi/10.1103/PhysRevB.90.161301>.
- [40] Shi Q, Zudov MA, Falson J, Kozuka Y, Tsukazaki A, Kawasaki M, et al. Hall field-induced resistance oscillations in MgZnO/ZnO heterostructures. *Physical Review B*. 2017 jan;95(4):41411. Available from: <https://link.aps.org/doi/10.1103/PhysRevB.95.041411>.
- [41] Yang CL, Zhang J, Du RR, Simmons JA, Reno JL. Zener Tunneling Between Landau Orbits in a High-Mobility Two-Dimensional Electron Gas. *Physical Review Letters*. 2002;89(7):76801.
- [42] Mori N, Ando T. Magnetophonon Resonance in Monolayer Graphene. *Journal of the Physical Society of Japan*. 2011 mar;80(4):44706. Available from: <https://doi.org/10.1143/JPSJ.80.044706>.
- [43] Perebeinos V, Tersoff J. Valence force model for phonons in graphene and carbon nanotubes. *Physical Review B*. 2009 jun;79(24):241409. Available from: <https://link.aps.org/doi/10.1103/PhysRevB.79.241409>.

- [44] Lindsay L, Broido DA. Optimized Tersoff and Brenner empirical potential parameters for lattice dynamics and phonon thermal transport in carbon nanotubes and graphene. *Physical Review B*. 2010 may;81(20):205441. Available from: <https://link.aps.org/doi/10.1103/PhysRevB.81.205441>.
- [45] Eaves L, Sheard FW. Size-dependent quantised breakdown of the dissipationless quantum Hall effect in narrow channels. *Semiconductor Science and Technology*. 1986;1(6):346–349. Available from: <http://dx.doi.org/10.1088/0268-1242/1/6/002>.
- [46] Wang L, Meric I, Huang PY, Gao Q, Gao Y, Tran H, et al. One-Dimensional Electrical Contact to a Two-Dimensional Material. *Science*. 2013 nov;342(6158):614 – 617. Available from: <http://science.sciencemag.org/content/342/6158/614.abstract>.
- [47] Kumaravadivel P. Private Communication; 2019.
- [48] Dean CR, Young AF, Meric I, Lee C, Wang L, Sorgenfrei S, et al. Boron nitride substrates for high-quality graphene electronics. *Nature nanotechnology*. 2010 aug;5(10):722–726. Available from: <http://www.ncbi.nlm.nih.gov/pubmed/20729834>.
- [49] Cheianov VV, Fal’ko VI. Selective transmission of Dirac electrons and ballistic magnetoresistance of n-p junctions in graphene. *Physical Review B - Condensed Matter and Materials Physics*. 2006 jul;74(4):41403. Available from: <https://link.aps.org/doi/10.1103/PhysRevB.74.041403>.
- [50] Das Sarma S, Adam S, Hwang EH, Rossi E. Electronic transport in two-dimensional graphene. *Reviews of Modern Physics*. 2011 may;83(2):407–470. Available from: <https://link.aps.org/doi/10.1103/RevModPhys.83.407>.
- [51] Vdovin EE, Mishchenko A, Greenaway MT, Zhu MJ, Ghazaryan D, Misra A, et al. Phonon-Assisted Resonant Tunneling of Electrons in Graphene–Boron Nitride Transistors. *Physical Review Letters*. 2016 may;116(18):186603. Available from: <https://link.aps.org/doi/10.1103/PhysRevLett.116.186603>.